CHARACTERIZATION OF ENCAPSULANT AND EDGE SEAL MATERIALS FOR FLEXIBLE SOLAR CELL PACKAGING

A Dissertation
Presented to
The Academic Faculty

by

Michael Carriell Sulkis

In Partial Fulfillment
of the Requirements for the Degree
Master of Science in the
School of Mechanical Engineering

Georgia Institute of Technology
May 2019

CHARACTERIZATION OF ENCAPSULANT AND EDGE SEAL MATERIALS FOR FLEXIBLE SOLAR CELL PACKAGING

Approved by:

Dr. Samuel Graham, Advisor
School of Mechanical Engineering
Georgia Institute of Technology

Dr. Suresh Sitaraman
School of Mechanical Engineering
Georgia Institute of Technology

Dr. C P Wong
School of Materials Science and Engineering
Georgia Institute of Technology

Date Approved: April 23, 2019

To my family and friends

ACKNOWLEDGEMENTS

I would like to express my sincere and deep gratitude to my advisor Dr. Samuel Graham for his guidance, encouragement, and support throughout my time here at Georgia Tech. I could always count on his expertise and experience to guide me through problems I faced. It has been a tremendous pleasure to be a member of his research group, and I am extremely grateful to have been given this opportunity.

I would also like to thank my committee members, Dr. Suresh Sitaraman and Dr. C.P. Wong for their advice and participation in this work.

This work would not have been possible without support from members of the C.P Wong research group, Jinho Hah, and Dr. Jack Moon. I would like express my particular appreciation to Jinho Hah. His endless help, materials science expertise, and friendship were hugely important to the success of this project.

I would also like to thank my collaborators Matthew Reese, Mike Kempe, Graham Colegrove, and Rosemary Bramante at the National Renewable Energy Laboratory for their support, helpful conversations, and for providing many samples to me. Additionally, support from Scott Jones at 3M, Sean Garner at Corning, and Doojin Vak at CSIRO-Monash is very much appreciated.

I would like to thank the current and past members of the Graham Lab for their assistance, camaraderie, and moral support over the years: Dr. Ankit Singh, Dr. Kyungjin Kim, Dr. Georges Pavlidis, Dr. Brian Foley, Luke Yates, Nicholas Hines, Zhe Cheng, Jason Hirschey, Gabe Cahn, Samuel Kim, Brian Kelly, Priyanka Deo, Jingjing Shi, and Dr.

Darshan Pahinkar. I would like to especially thank Dr. Ankit Singh for his time spent bringing me up to speed when I arrived and for teaching me a great deal along the way.

I acknowledge financial support from the Durable Module Materials (DuraMAT) consortium, part of the Energy Materials Network sponsored by the U.S. Department of Energy.

Last but certainly not least, I want to thank my family and friends for their love and support during my time at Georgia Tech. To my parents especially, their constant support has meant so much to me.

TABLE OF CONTENTS

LIST OF TABLES

LIST OF FIGURES

LIST OF SYMBOLS AND ABBREVIATIONS

E	Young's modulus
G_c	strain energy release rate
G_{th}	strain energy release rate (Griffith's criteria)

PV	photovoltaic
OSC	organic solar cell
PCE	power conversion efficiency
EVA	ethylene vinyl acetate
PIB	polyisobutylene
PDMS	Polydimethylsiloxane
PET	polyethylene terephthalate
WVTR	water vapor transmission rate
RH	relative humidity
DH	damp heat
XPS	X-ray photoelectron spectroscopy

SUMMARY

Flexible photovoltaic technologies have the potential to produce lightweight, low-cost, and flexible devices as opposed to rigid conventional PV technologies. However, the acceptance of flexible devices by industry is hindered by reliability concerns. All PV technologies are sensitive to environmental factors like moisture, heat, and UV radiation, but this sensitivity is exacerbated for thin-film technologies. To ensure good reliability and lifetime, barrier materials must be used to prevent the ingress of moisture. Additionally, the device must be mechanically robust and resist delamination. For traditional PV technologies, this is accomplished using encapsulants and edge seals. These materials, when used together, provide sufficient moisture protection as well as mechanical support to mitigate moisture ingress and mechanical damage. However, the development of flexible PVs has not been conducted with a parallel focus on packaging, and the optimal packaging strategy has yet to be determined. Therefore, this work seeks to investigate the moisture ingress and adhesion properties of a variety of encapsulant and edge seal materials that may be applicable for use in flexible PV packaging.

First, the moisture ingress properties of a variety of encapsulant and edge seal materials was evaluated using optical calcium degradation experiments with an improved automatic measurement system. Next, the best performing materials were used in mechanical adhesion experiments to evaluate initial strength and to investigate degradation due to accelerated aging conditions. Finally, chemical analysis was performing on the delaminated surfaces to investigate the underlying mechanisms. Together, the

characterization techniques used in this work provided valuable insight into the performance of flexible PV packaging materials.

CHAPTER 1. INTRODUCTION AND BACKGROUND

1.1 Overview and Motivation

The most recent NREL Solar Industry Update reports that by the end of 2017, the global capacity of photovoltaic (PV) installations reached 415 GW-DC, an increase of 98 GW-DC from 2016. It is reported that in 2017, 32% of all new electricity generating capacity in the U.S. came from solar installations [1]. Additionally, authors from the European Commission Joint Research Center report that new solar PV installations accounted for 6.86 GW of new capacity in 2015, 25% of all new installed capacity [2]. With this trend expected to continue in to the future [3], it is clear than the PV industry will play a critical role in the global energy marker for decades to come.

While conventional PV technologies are driving the growth of the industry [1], new technologies such as organic polymer-based, flexible devices are becoming increasingly popular in recent years. Organic solar cells (OSCs) in particular offer a low-cost, light-weight, and flexible option. The ability to manufacture these devices using low temperature, solution-based, vacuum-free processes is the main area of cost savings [4, 5]. However, most work in the area of organic and polymer solar cells has been focused on improving the power-conversion efficiency (PCE), while the long-term reliability of these devices generally falls far short of the requirements needed for economic production [6-9].

Utility PV installations are expected to maintain performance for a 20-30 year lifetime [3], and a significant amount of work has been conducted to understand the relevant degradation mechanisms of these devices [10-12]. For example, both moisture

ingress and loss of adhesion have been identified as primary failure mechanisms that can severely impact device lifetime if left unmitigated. The flexible PV industry, with fewer decades of development and a lack of long-term fielded modules, lags behind in terms of reliability.

1.2 Materials for Flexible Photovoltaics Packaging

Conventional solar cells are typically constructed in architectures similar to the diagram shown in Figure 1 below. An active layer, usually mono or multi-crystalline silicon, is laminated between two encapsulant layers, with a thick glass superstrate and a protective backsheet. An edge seal is also included around the perimeter. Depending on the specific design and application, modules may also be supported with an aluminum or plastic frame.

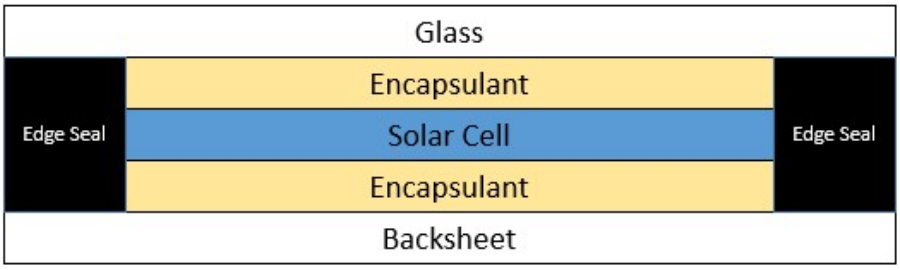

Figure 1: A simplified solar cell architecture.

As far as reliability is concerned, the encapsulant layer and edge seal materials are particularly important because they must provide both environmental and mechanical protection to the module. Encapsulant materials are required to protect modules from moisture, rain, ultra-violet (UV) radiation, and mechanical stress [13]. Other important properties of the encapsulant material are light transmission, adhesion, electrical insulation, and mechanical strength. The most commonly used encapsulant material is ethylene vinyl

acetate (EVA), which has been used extensively in PV modules for the past 30 years. Other less commonly used encapsulant materials include silicones, ionomers, thermoplastic polyurethane (TPU), polyvinyl butyral (PVB), and polyolefins [14].

Edge seal materials are a critical component of the typical PV module architecture, with much of the work characterizing their performance occurring in the last decade or so. Edge seals are important because, while the front and back sheets can be made of impermeable materials, moisture can still diffuse through the sides of the module relatively easily [12, 15]. Therefore, a low moisture permeability material is often included around the perimeter of modules to prevent this "side permeation" of moisture.

Besides encapsulant and edge seal materials, other flexible materials are being developed for use in PV module packaging. These include flexible top layers such as flexible glass or laminate structures containing thin film barriers. One flexible glass option that is currently available on the market is Willow^{TM} Glass by Corning. Willow^{TM} Glass offers a perfect hermetic barrier that can be applied in a roll-to-roll process, and some work has been done using this material to encapsulant PV devices [16, 17]. 3M has also produced a flexible top sheet material with their Ultra Barrier Solar Film. This material is uses a PET substrate and a fluoropolymer top layer to sandwich a barrier layer, and has a reported WVTR of $<7.00 \times 10^{-3}$ g/m^2/day. Additionally, researchers at the Holst Centre have developed flexible barrier technology aimed at both the OLED and flexible PV industry. Their approach, using silicon nitride and an organic planarization layer in a SiN/Organic/SiN laminate, was estimated to have a WVTR below 10^{-6} g/m^2/day at ambient conditions while also being flexible to a 20mm minimum bend radius [18]. This work on

flexible barrier films has been also been implemented in recent work developing flexible, roll-to-roll processed solar cells [19-21].

1.3 Device Degradation

The degradation of silicon PV modules due to environmental exposure is well documented [3, 22-27], and the most prevalent failure modes for fielded PV modules are summarized below in Figure 2.

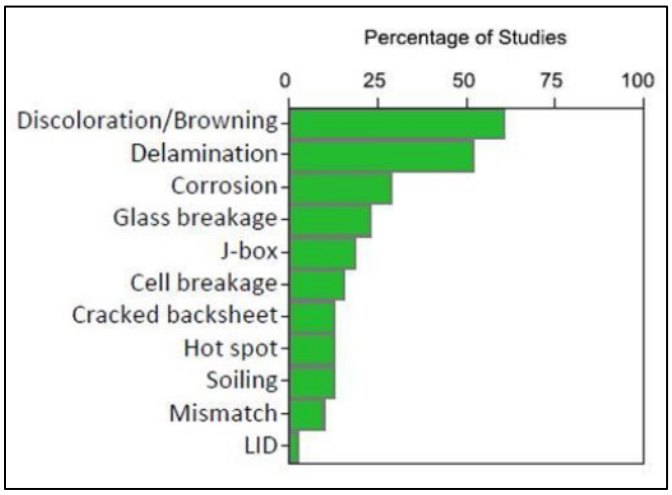

Figure 2: Failure modes in fielded PV modules [27].

Moisture intrusion into a PV cell through the sides or through permeable layers can cause corrosion of metallization and semiconductor materials which diminishes electrical performance. Additionally the retention of moisture in a cell increases the packaging materials electrical conductivity, increasing leakage current and further decreasing electrical performance [11]. An example of corrosion due to moisture ingress is shown in Figure 3 below.

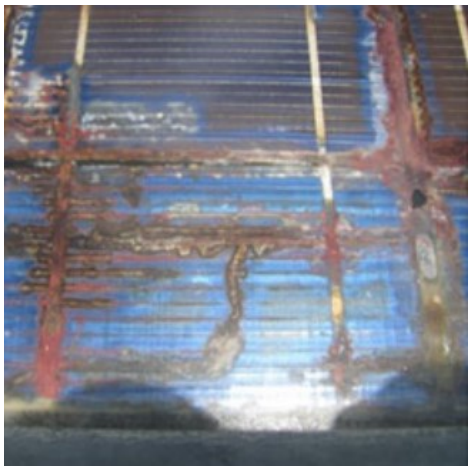

Figure 3: Corrosion of a PV module due to moisture ingress. Adapted from [26].

In addition to moisture permeation through the module materials, delamination is mechanism in which moisture can penetrate a device. Wohlgemuth *et al.* note that delamination between the cell and the commonly used EVA encapsulant is the most common observation, while instances of glass/EVA delamination are fewer. These authors also report several causes of EVA/cell delamination including flux residue, inadequate EVA coverage, leakage-current induced reactions, and metallization catalyzed reactions. [27]. Other work by Jorgensen *et al.* investigated EVA/Glass adhesion. In this work it was found that moisture can interact with the silane coupling agents often used in as adhesion-promoters often used in EVA formulations. This causes a condensation and reverse hydrolysis reaction. In the presence of enough water, the hydrolysis reaction dominates and adhesion strength suffers [28]. An example of delamination in a PV module is shown in Figure 4 below.

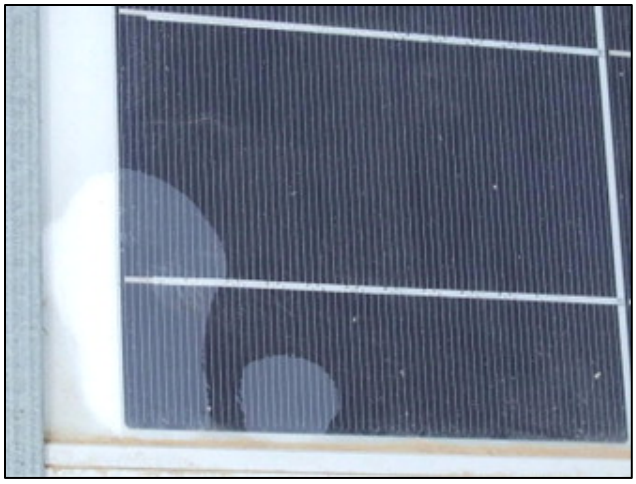

Figure 4: A PV module with delamination [29].

Since flexible thin film technologies have active layers on the order of 1-µm thick, the perceived risk is high than for crystalline silicon modules with thicker, more durable layers. Therefore, the risks associated with the failure modes shown in Figure 2, especially delamination and corrosion, are heightened for thin film flexible modules.

1.4 Efforts to Improve Reliability

Recently, several groups have identified areas in which more work concerning reliability of PV modules would be valuable to the field. Building on the body of data concerning moisture permeation and delamination described previously, several studies concerning moisture ingress into PV modules, as well as studies investigating the adhesive performance of these materials have been performed.

1.4.1 Moisture Permeation

Work by Kempe *et al.* addresses the concern that while a module can be constructed using impermeable glass front and back sheets, moisture can still permeate through the sides of the device. Using an optical technique, which will be described in greater detail in

the Chapter 3, it was found that desiccant-filled polyisobutylene (PIB) edge seal materials exhibit far better moisture permeation properties than the best low-diffusivity encapsulants. This material has been shown to provide excellent barrier performance (WVTR on the order of $5x10^{-5}$ g/m^2/day at ambient conditions), while also being useable in low-temperature lamination processes [30]. Kempe *et al.* showed that a 1cm strip of this PIB edge seal will limit moisture ingress to the perimeter of the device over a 20 year lifetime, while permeation through the encapsulants may more rapidly extend across the entire module [31, 32]. An example of encapsulant materials being evaluated by this group is shown below in Figure 5.

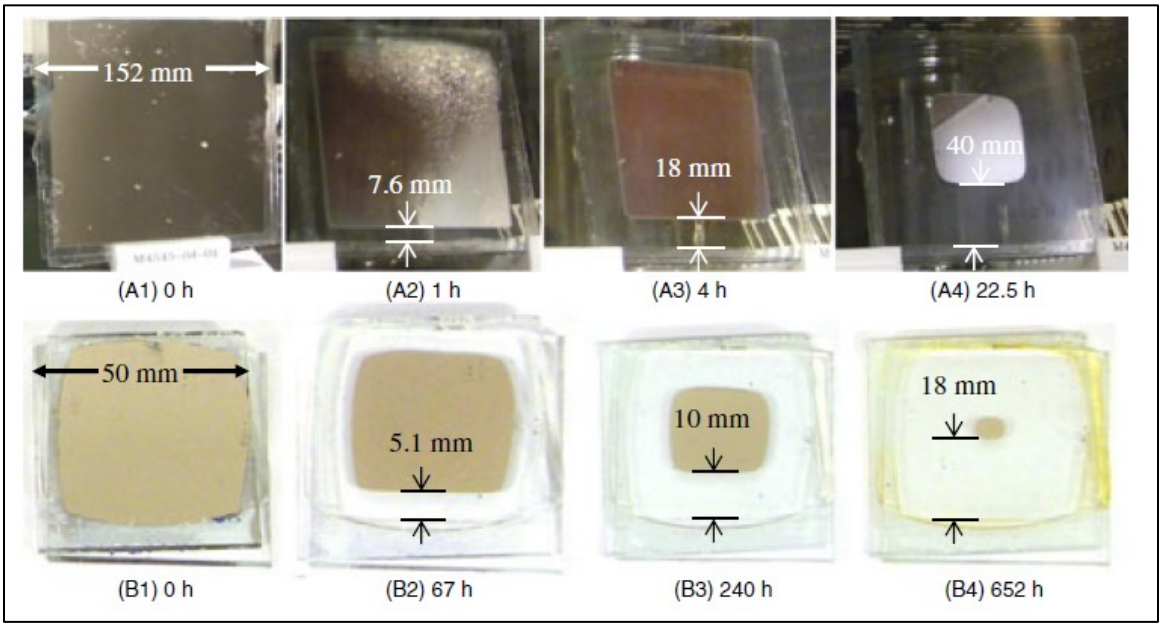

Figure 5: Encapsulant materials being evaluated for moisture ingress. Adapted from [31].

1.4.1.1 Barrier Films

In addition to evaluating encapsulant and edge seal materials, significant amounts of work have been done investigating barrier film technology. Barrier films are attractive

because, if the film can provide meaningful environmental protection, then the lightweight and flexible properties of thin-film PV technology can be maximized. An extensive analysis of barrier films and their reliability is presented by Hyung Chul Kim in his 2015 dissertation [33], and details relevant to this thesis are summarized in this section.

Barrier films can be produced in several ways including Plasma Enhanced Chemical Vapor Deposition (PECVD), sputtering, and Atomic Layer Deposition (ALD), and these methods are often combined to create multilayer laminates. Films made with these methods have been shown to exhibit ultra-barrier properties with water vapor transmission rates (WVTR) less than $1x10^{-4}$ g/m^2/day. However, there are many challenges associated with using films to packaged devices including particle defects and cracks that impact the barrier properties.

The permeation of gas through a barrier film is governed by the intrinsic permeability of the film, as well as the defect-related permeation; both mechanisms can be combined into an effective diffusion coefficient. An illustration of the different permeation mechanisms is shown in Figure 6 below.

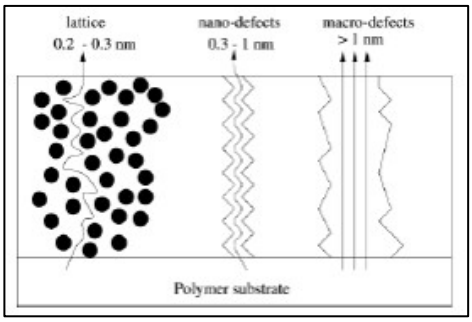

Figure 6: Permeation mechanisms through a barrier film. Adapted from [33].

Kim demonstrated that a fracture mechanics based approach can be used to produce more reliable barrier films. It was shown that multilayer laminates of polymers and

inorganic layers can be engineered to mitigate the effects of particle defects while also providing good barrier performance. Kim's work also investigated the chemical stability, electrical properties, and gas barrier properties of thin ALD films, and their utility as a device encapsulant was demonstrated. However, a lifetime study on devices constructed using these films was not conducted. While barrier film technology shows significant potential for providing ultra-barrier performance in a thin form factor, additional work optimizing the performance and improving the manufacturability is needed.

1.4.2 Adhesion

As described previously, delamination in a module can have severe impacts on the electrical performance, and several recent studies have sought to broaden the understanding of this phenomenon. Bosco *et al.* report threshold values of encapsulant and backsheet adhesion using a modified cantilever-beam method to evaluate the critical debond energy G_c. In their work, a width-tapered substrate (illustrated in Figure 7) is used to propagate delamination between module packaging layers. The benefits of this method are that it can be implemented on both full-sized modules as well as engineering coupons, and the method allows for rapid evaluation of G_c. The study addressed delamination concerns most relevant to conventional, rigid PV modules, and reports threshold G_c values for encapsulants and backsheets of ~160 J/m^2 and ~10 J/m^2 respectively [34-36].

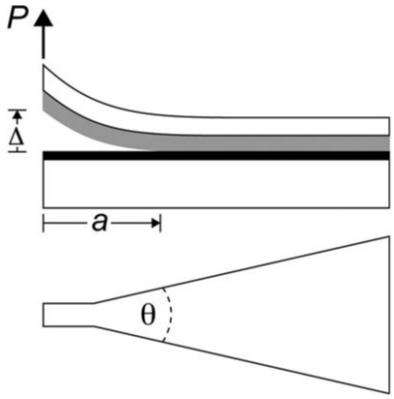

Figure 7: A diagram of the width tapered cantilever beam developed by Bosco *et al.* [35].

Other studies related to adhesion investigate the effects of environmental exposure [27, 37-40]. These studies, which include thermal, humidity, and UV aging studies seek to quantify the degradation of adhesive performance over time. Work by Wohlgemuth *et al.* investigated the effects of all three exposure conditions on the strength of EVA/Glass bonds. Their results, shown in below, clearly show a decrease in adhesion due to UV exposure as a function of temperature. Additionally, increasing the relatively humidity from 30% to 50% produced the same effect as increasing the temperature from 60°C to 80°C.

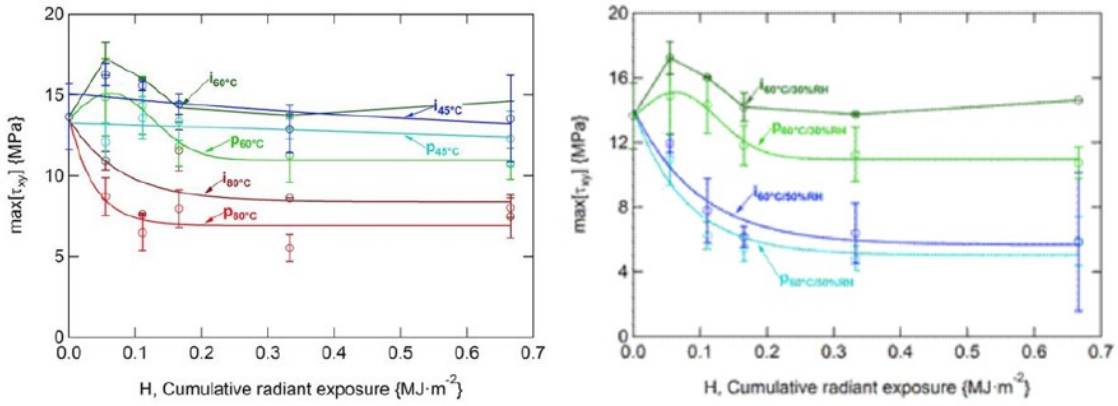

Figure 8: The degradation of EVA/Glass adhesion under UV, thermal, and damp heat conditions [27].

Work by Cai *et al.* investigated the degradation of silicone (PDMS) encapsulant under UV conditions. This work, while aimed at solar concentrator applications, is still relevant to the community at large and also includes chemical analysis of the delaminated surface to further investigate the failure mechanisms. The reported behavior of silicone encapsulant bonded to glass substrates is shown in Figure 9 below. The results show an initial bump in adhesion energy followed by a decline, and elevated temperature accelerates this process. This group then analyzed the delaminated surfaces using X-ray Photoelectron Spectroscopy (XPS) and transmission Fourier-Transform Infrared Spectroscopy (FT-IR). The increase in adhesion was attributed to an increase in the number of bonds at the interface. It was also found that the failure mode changed from adhesive with no UV exposure to cohesive with increased UV exposure. FT-IR analysis indicated that increased crosslinking in the bulk silicone resulted in an increase in G_c.

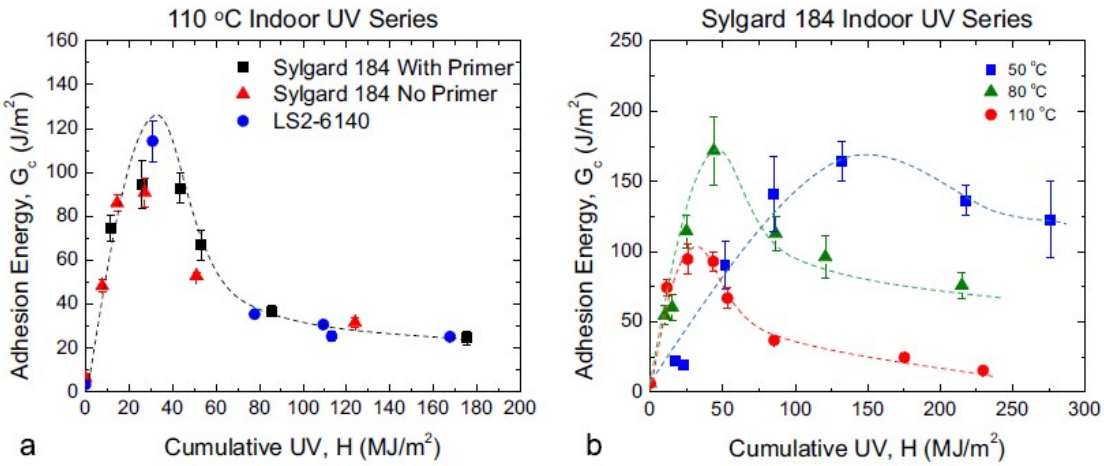

Figure 9: The degradation of PDMS/Glass adhesion under UV exposure [37].

While most work has focused on the properties of encapsulants, significantly less attention has been paid to the mechanical and adhesive properties of edge seals. However, the results of moisture permeation studies [31, 32] indicate that the adhesive performance of edge seals is critically important. Without sufficient adhesion strength edge seals may easily delaminate and allow significant moisture ingress through the sides of the module. To address this, some very recent studies have sought to investigate the adhesive performance of PIB based edge seals [39, 40].

The first study by Kempe *et al.* investigates a wedge-adhesion test similar to the Boeing wedge test, also known as the Wedge Cleavage test [41]. This method, illustrated in Figure 10 uses a small stainless steel rod to wedge apart glass substrates bonded together with edge seal material, the resulting delamination slowly propagates and is measured. Using the measured crack length (a) and known parameters including the plane strain Young's modulus (E), the thickness of the beam (t), and the difference between the wedge thickness and the adhesive thickness (h), debond energy G_{th} can be calculated using Equation 1.

Figure 10: A diagram of the wedge adhesion test used to evaluate edge seal adhesion. Adapted from [39].

$$G_{th} = \frac{3Et^3h^2}{16a^4} \quad (1)$$

However, the authors note that the preponderance of PIB materials to fail cohesively and the ensuing uncertainty limits the usefulness of this method. Therefore, the authors suggest other methods of evaluating PIB edge seal materials including a butt-joint test. This method, published very recently, uses Glass/PIB/Glass test specimens (illustrated in Figure 11) adhered to large elevator bolts using epoxy. The bolts are then pulled apart at a specified rate, and the maximum stress is recorded. Additionally, the failure mode was assessed after testing, and the amount of cohesion (%area) is recorded.

Figure 11: Some examples of Glass/PIB/Glass samples tested using the butt-joint adhesion method [40].

In recent years the development of polymer-based flexible solar cells has also led to the investigation of adhesion in thin-film layers. For example, Dupont *et al.* studied the adhesion properties in roll-to-roll processed inverted polymer solar cells. In her work, low adhesion was reported between the bulk heterojunction layer and the adjacent conductive polymer layer, and strategies for improving this interface were explored [42, 43]. In similar work, failure within the active layers of perovskite based solar cells has been explored. In

work by Rolston *et al.,* a variety of perovskite device architectures are used to investigate the effects of both deposition technique and chemistry on interlayer adhesion. Their results showed that initially poor fracture energy (~1.5J/m^2) could be modestly improved using such methods as maximizing perovskite grain size, and incorporating a mesoporous scaffold in the perovskite layer to improve the mechanical properties of the resulting films [44]. Additionally, efforts to understand the role of device encapsulant on the thermomechanical reliability of perovskite films has been conducted by Cheacharoen *et al*. In their work, two different encapsulant materials, EVA and an ionomer based material, were investigated. It was found that the using the softer EVA encapsulant resulted in 90% performance retention over 200 temperature cycles, while using the stiffer ionomer material resulted in delamination and a drop in performance [45].

1.5 Summary

It is clear from the available literature that the reliability of PV modules is still a primary concern. Delamination subsequent corrosion continue to impact module performance, and mitigating these issues will help to increase the adoption of solar technology. However, the vast majority of work has been conducted with conventional, rigid, modules in mind, which makes sense given the current share of the market that conventional PV occupies. However, as new flexible thin film PV technologies are being developed, there is a lack of understanding of the performance and degradation of the materials used in these new packaging architectures. Therefore, there is a substantial need to investigate the materials used in flexible PV packaging in order to develop functional and reliable devices.

1.6 Objectives and Scope

Based on the clear need for further work on the reliability of flexible photovoltaics, this research will seek to improve the lifetime of these devices by investigating some of the critical mechanical properties, namely moisture ingress and adhesion. The structure of this work is as follows:

- Chapter 2 investigates the moisture permeation properties of a variety of commonly used PV encapsulant and edge seal materials using optical calcium corrosion measurements. An assessment of the performance of the materials will be detailed, with the conclusions providing direction for the subsequent work on adhesion.
- Chapter 3 investigates the mechanical performance of encapsulant and edge seal materials in adhesively bonded architectures. High performing materials from initial measurements are also subjected to a suite of aging studies, where their long term performance under various environmental conditions are evaluated.

Finally, Chapter 4 summarizes the progress made and contributions of this thesis. Chapter 4 also suggests future work that can provide further insight into the performance and behavior of the materials under investigation.

CHAPTER 2. MOISTURE PERMEATION THROUGH ENCAPSULANTS AND EDGE SEALS

2.1 Introduction

As described in the previous chapter, the moisture barrier performance of materials used in photovoltaics packaging is critical for device lifetime. Therefore, implementing methods to characterize the mass transport properties of water vapor in encapsulant and edge seal materials is essential.

2.2 Materials

In this work, a variety of commercially available encapsulant and edge seal materials were selected for evaluation. Additionally, some effort was put into developing novel encapsulant formulations. In any case, the majority of the materials investigated commercially available options formulated for PV applications.

2.2.1 Encapsulants

Several polydimethylsiloxane formulations were acquired for this research. The first Qsil 216 (Quantum Silicones) is a two-part, transparent, thermally cured encapsulant. This material is advertised to contain a non-yellowing catalyst system, and to provide hydrolytic stability and reversion resistance [46]. The second PDMS used in this work (2538, H.B. Fuller) is a transparent addition cure silicone offering high optical transmission [47]. The final PDMS material investigated here is the PV-6212 Cell encapsulant from Dow Corning.

This material is again a two-part addition cure silicone advertising UV stability, excellent humidity resistance and high optical transmission [48].

An ethylene vinyl acetate (EVA) copolymer was also used in this work. As mentioned previously, EVA is the most widely used encapsulant material in the industry. However, several known issues such as yellowing and acetic acid production present long-term reliability concerns. The specific formulation used here, PHOTOCAP 1550P (STR Solar), is an ultra-fast cure formulation provided as a film. Additionally the material is self-priming for improved glass adhesion [49].

An ionomer based encapsulant, PV5400 (DuPont), was also chosen for this work. Ionomers are a relative newcomer to the PV encapsulation field, but manufacturers claim to that they provide superior moisture ingress resistance, increased module strength, and no acetic acid production [50].

The last class of encapsulant materials investigated in this work is polyisobutylene (PIB) rubbers. While PIB is typically used an edge seal material, transparent formulations could provide an alternative to the other commonly used encapsulant materials. For this work, both low and a high molecular weight (MW) transparent PIB formulations (Oppanol® B 11 SFN and Oppanol® N 50 SF) were used in experiments. It was found that the low MW formulation had good flow properties, but the high MW PIB was too stiff to be useable in the experiments described later. Therefore, a 1:3 blend of the two formulations was produced to investigate the role of molecular weight on performance.

2.2.2 Edge Seals

The only edge seal material investigated here is the PVS101 (also known as ADCO) by Royal Adhesives and Sealants. This material is a PIB base that has been loaded with reactive desiccant. The material is also stabilized with carbon black, so it is completely opaque and is therefore only useable as an edge seal [51].

2.3 Optical Calcium Corrosion Test

The optical calcium test was first developed by Nisato *et al.* as a measurement technique for low H_2O permeation rates. The method has since become popular for measuring moisture permeation through barrier materials because of its very high sensitivity. Compared to other high-performance methods, the optical calcium test exhibits the lowest detection limit for water vapor transmission rate (WVTR) measurements of $<1x10^{-6}$ g/m^2/day [52, 53]. The test relies on the rapid reaction between water and calcium shown in Equation 2 below.

$$Ca + 2H_2O \rightarrow Ca(OH)_2 + H_2 \quad (2)$$

Calcium, which is initially opaque and mirror-like, reacts with water to produce optically transparent calcium hydroxide [54]. Therefore, by measuring the degradation of calcium in a representative architecture, one can determine the amount of moisture ingress through a barrier material. The architectures used in this work is shown in Figure 12 below. A thin layer of calcium deposited on a glass substrate is encapsulated with a moisture barrier material under investigation and capped with a transparent barrier layer.

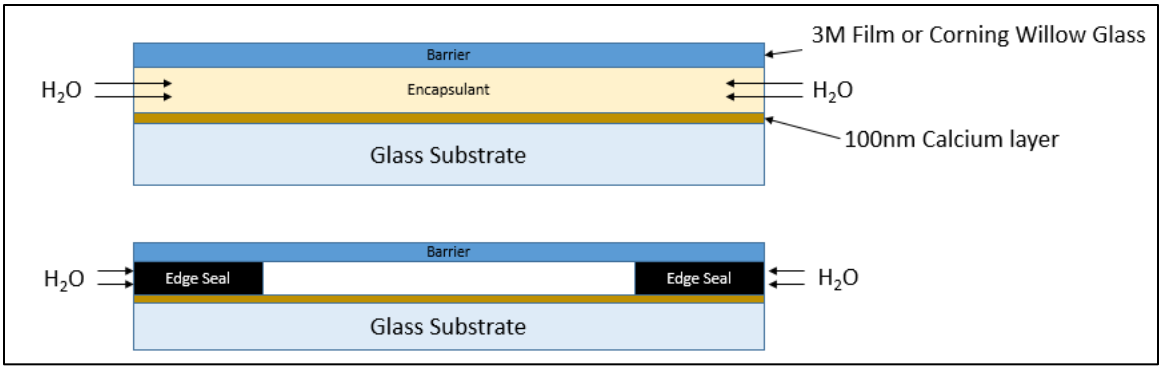

Figure 12: Optical calcium sample architectures for encapsulant (top) and edge seal (bottom) materials.

By using an impermeable barrier layer such as glass, the moisture ingress can be restricted to side permeation through the encapsulant or edge seal material. This method of measuring side ingress was developed by *Kempe et al.* and has proven its utility for measuring the moisture permeation characteristics of PV encapsulant and edge seal materials. In their work, a variety of encapsulant and edge seal materials were evaluated for moisture barrier performance in side permeation architectures and their results are shown in below [15, 25, 31, 32].

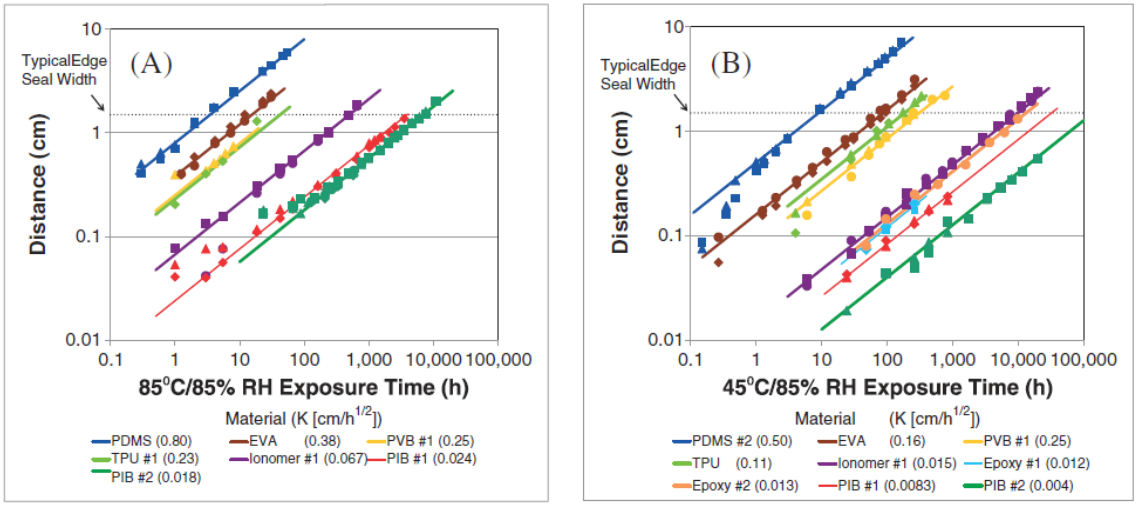

Figure 13: Moisture permeation distance versus exposure time results for encapsulant and edge seal materials at (a) 85°C/85%RH and (b) 45°C/85%RH [31].

It should be noted that the specific products or formulations used in this work are not reported beyond basic details. It was found that the best performance at both conditions came from a desiccant-filled PIB formulation, and the worst performance was from a PDMS. Notably, the most popular PV encapsulant material, EVA, only performed slightly better than the worst performing PDMS. The ionomer formulation was the best performing non-PIB or epoxy material studied in their work. Comparisons to this data will be made in the results section of this work.

2.3.1 Sample Fabrication

For this work, calcium test substrates fabricated according to the procedure described in [31] were provided by the National Renewable Energy Laboratory (NREL); a photo of a typical specimen is shown in Figure 14 below.

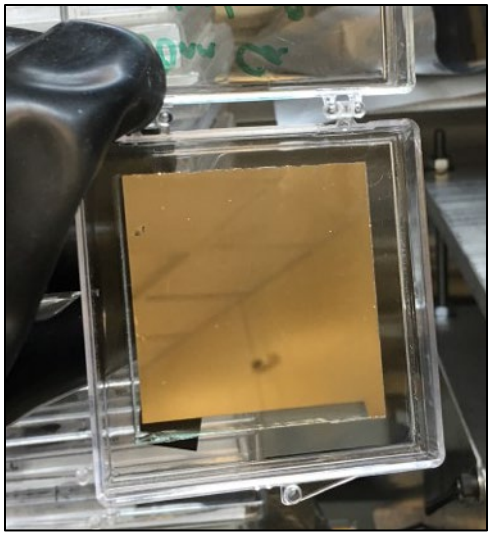

Figure 14: A calcium test card provided by NREL.

The calcium substrates were shipped in sealed and desiccated containers and were immediately transferred into a dry N_2-filled glovebox upon arrival. The samples were then inspected to verify their quality and ensure no degradation occurred during shipping. Glass cover slides were prepared by scrubbing with detergent (Alconox Inc.) followed by rinsing with acetone and isopropanol (IPA), and dried under a compressed air stream. The glass cover slides were stored in the glovebox to dry for at least 1 week prior to use. Polymeric materials used in these experiments were also stored in the glovebox for at least 1 week prior to use to ensure that no residual moisture remained in the materials. The lamination of the materials was performed using a hot plate and a small pneumatic press stored inside the glovebox. The design of the pneumatic press is described in the following section. Each sample structure consisting of a calcium card, encapsulant material, and cover glass was assembled by hand on the hot plate, where it was heated to between 100°C and 150°C depending on the encapsulant manufacturer's specification. Additionally, a fluoropolymer-coated sheet was inserted between the calcium sample and the glass cover slide as a spacer to keep the slides parallel and separated at a distance of approximately 0.125mm. After

heating, samples were quickly transferred to the pneumatic press where sufficient pressure was applied to laminate the materials. An illustration of this process is shown in Figure 15 below.

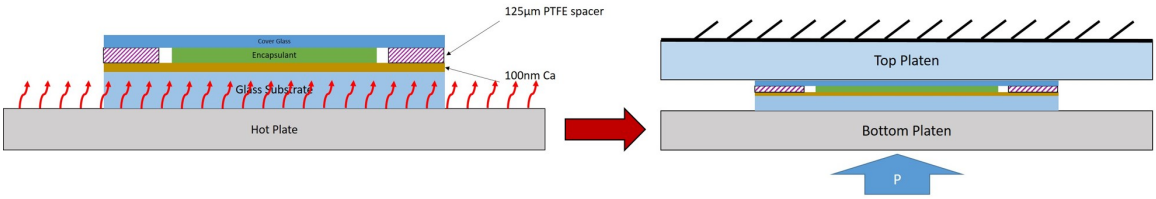

Figure 15: The process of assembling and heating a calcium sample on a hot plate, and lamination on the press.

Laminations were visually inspected during and after the lamination step to verify that major defects were present, and good "flow" was achieved. After lamination, samples were allowed to cool overnight in the glovebox. A photo of two finished samples, one made from the black ADCO polyisobutylene edge seal and one from a transparent PDMS, is shown in Figure 16 below.

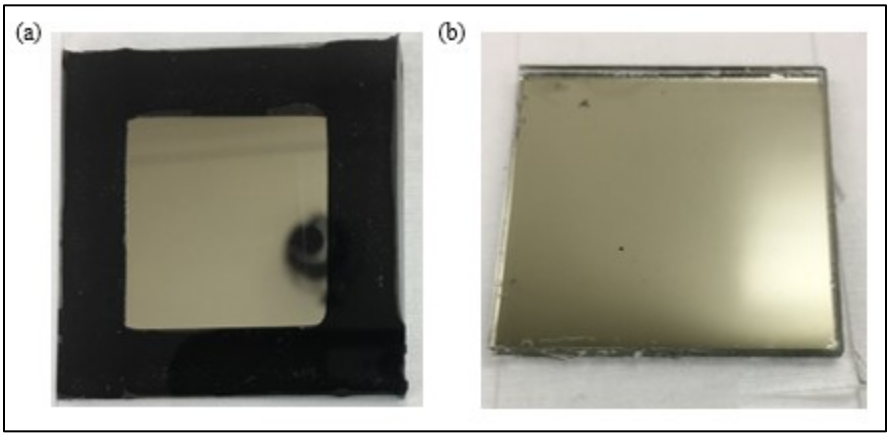

Figure 16: Finished optical calcium samples of (a) PIB edge seal and (b) PDMS encapsulant.

2.3.2 Pneumatic Press Design

Initially, optical calcium test samples were fabricated using a hand assembly procedure which involved applying lamination pressure using a small rubber hand roller. However, this method had repeatability issues because it was impossible to both maintain a consistent lamination pressure across a sample, and to perform identical laminations across a multiple samples in a set Therefore, the need for an adjustable and repeatable lamination method was clear. With recommendations from collaborators at NREL, a small pneumatic press was designed that could easily be stored inside a glovebox, could provide sufficient lamination pressure, and could provide repeatable results. The final design, shown in Figure 17 below, consists of an aluminium frame, a small pneumatic cylinder, gas plumbing, and platens.

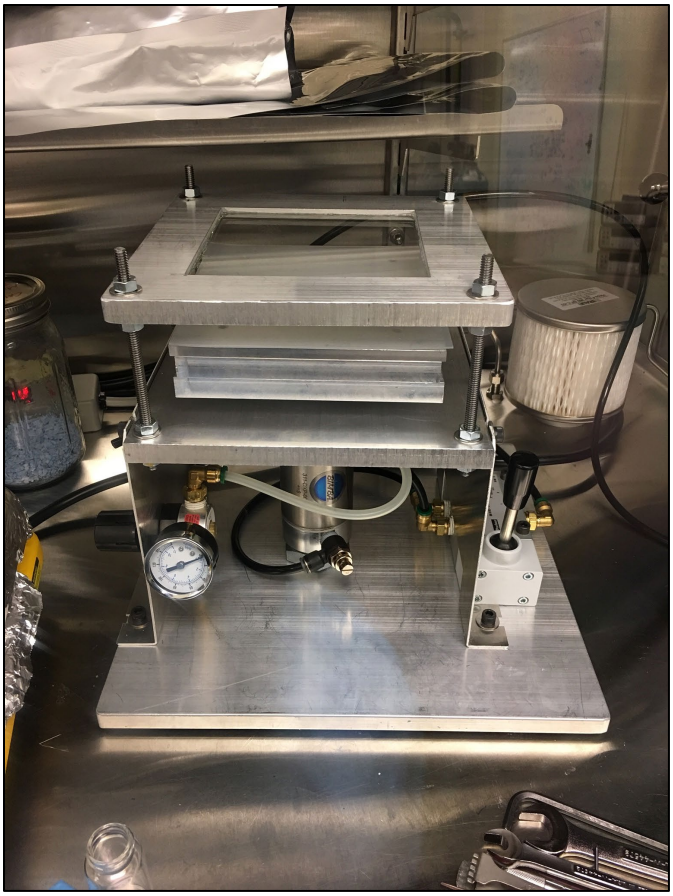

Figure 17: The pneumatic press built for optical calcium sample fabrication.

The gas plumbing system for the press is relatively simple, with some features for safety. High purity nitrogen is plumbed into the glovebox at approximately 120psi, and is then reduced to 65psi by the control valve visible in Figure 17. Following pressure reduction, the nitrogen is piped through an On/Off switch valve and a joystick control valve. The piston follows after the control valve. The On/Off switch and the control valve must be operated in unison to actuate the piston which requires two-handed operation. This prevents the user from actuating the piston while their hands remain between the platens.

The main characteristic of the design that make this press well suited to optical calcium sample fabrication is the transparent top platen. This allows for the sample to be visually inspected during the lamination processes, which, as described previously is

important for ensuring proper lamination pressure and hold time. Finally, a thin silicone rubber mat is placed on the bottom platen providing a compliant surface. This helps to improve coplanarity between the sample layers and also cushions the sample during lamination. A schematic of the press platens is illustrated in Figure 18.

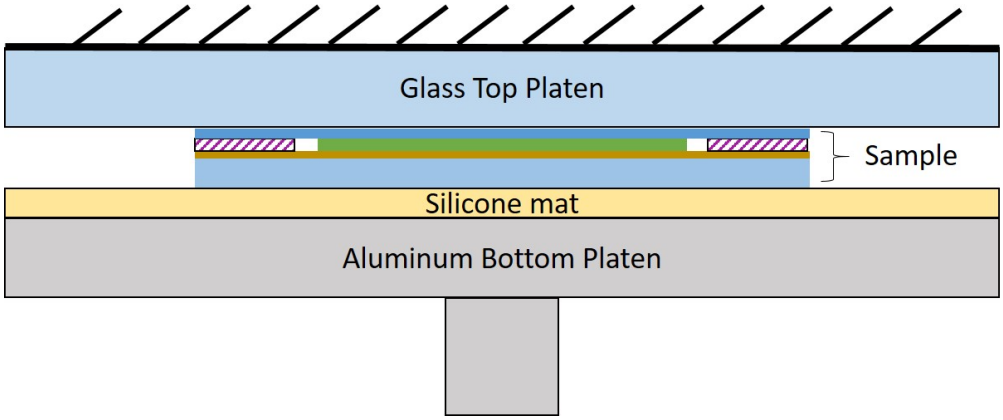

Figure 18: A diagram showing the glass top platen and the silicone mat used in the pneumatic press design.

2.3.3 Damp Heat Aging

After samples were manufactured, they were aged in 85C/85%RH conditions, which is a commonly used accelerated aging condition for PV modules and materials, and is included in IEC61215 standards for PV module qualification. Therefore, this condition was selected for screening of flexible PV materials in this work.

The damp heat environment was created using a benchtop environmental test chamber (MicroClimate, Cincinnati SubZero, Inc. Figure 19(a)). The samples were placed in the chamber in a holding rack that held the samples upright (Figure 3(b)). This orientation was found to be important because it limited the accumulation of condensation on the samples, which leaves residue that disrupts optical measurements. The samples were periodically removed from the chamber and images were taken using a high-resolution

flatbed photo scanner (Epson, Figure 20). The scanner consists of a CCD image sensor, a white LED light source, and a white back-reflector. The scanner software was configured to take color photos at 2400dpi with no color correction. Given this resolution, the theoretical sensitivity of the scanner measurements is 0.01mm, which is a significant improvement over hand measurements. Immediately after scanning the samples were returned to the environmental chamber, with the total excursion time out of the environmental chamber being approximately 1-2 minutes. Sample degradation was then measured using an automated measurement tool in MATLAB, which is described in the following section.

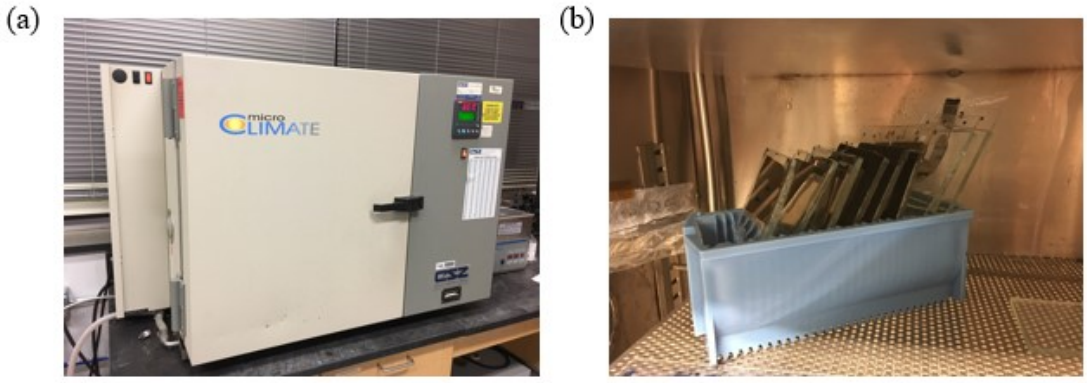

Figure 19: (a) Benchtop environmental chamber (MicroClimate, Cincinnati SubZero, Inc.). (b) Calcium test samples in sample rack during testing.

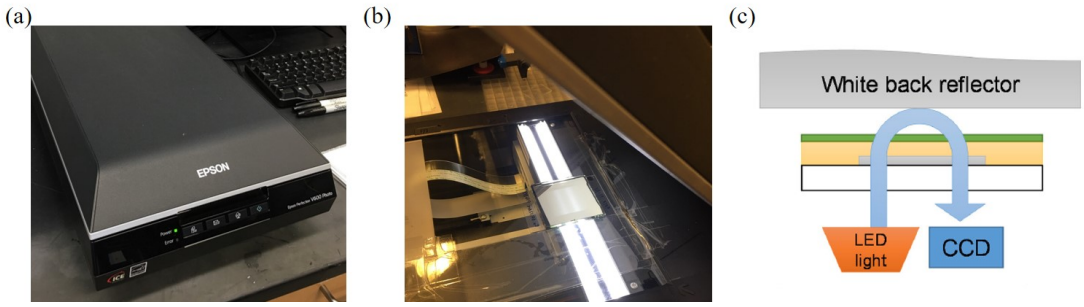

Figure 20: (a) A flatbed photo scanner, Epson V800 (Epson), (b) a sample being scanned with the top open for illustration and (c) the operation of the scanner while imaging calcium samples.

2.3.4 Automated Degradation Measurements using MATLAB

Previous work by Kempe *et al.* relied on manual measurements of degradation distance in order to quantify the barrier performance of encapsulation materials. However hand measurement becomes extremely tedious for large sample sets and lengthy experiments. Additionally, high performing materials degrade very slowly, which means the change in visible calcium from one measurement to the next is often minute. Since the reported uncertainly of the hand measurement technique is ±0.5mm, accurate measurements of high performing materials may be difficult to achieve [31]. Therefore, an automated, higher resolution technique for measuring calcium degradation distance is quite valuable for both increasing measurement through-put and reducing the uncertainty of results.

The general algorithm designed for the calcium measurement process is as follows: binary conversion, alignment, and measurement. Images taken using the flatbed photo scanner during the experiment were first converted to binary images. This is performed by first converting the images to grayscale and calculating an intensity threshold. Image pixels with an intensity value above the threshold are then remapped to 1, and image pixels with

an intensity value below the threshold are remapped to 0. The intensity threshold value was determined by Otsu's method using a built-in MATLAB function [55]. An example of the binary conversion of an optical calcium sample image is show in Figure 21 below; the calcium area is clearly defined against the white background.

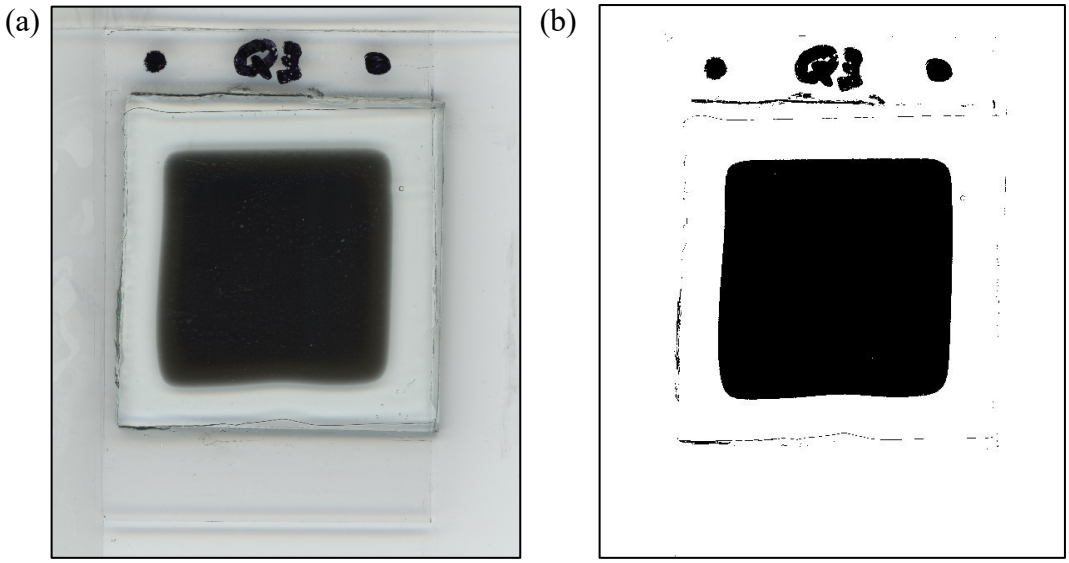

Figure 21: A full color image (a) of a calcium sample is converted to a binary image (b).

Following binary conversion, the next step in the processing algorithm was alignment. Proper alignment of the entire set of images allows for a simple measurement loop to be implemented for each image without requiring additional input. Alignment is performed using markers made with permanent marker on each sample. The markers, shown in Figure 21, are detected using a feature-detection sub-routine which locates the centroids. Using the first image as a template, the translational error of each subsequent image was determined by calculating the distance between the centroids of the same marker across two images. The rotational error was calculated by measuring the angle between the two markers on a single image with respect to horizontal. With both translational and

rotational error known for each image, a perfectly aligned stack of images was generated for each sample.

Once the images were aligned, the measurement sub-routine was executed. For the first image, a region of interest (ROI) was superimposed over the calcium sample that completely encompassed the calcium area, and the centroid of the calcium area was calculated. Then for each image, the size of the calcium was calculated as the distance from the original centroid location to the edge of the calcium area in each direction. This distance was determined by leveraging the binary nature of the images, where pixels values of zero correspond to calcium, and pixels values of one correspond to transparent calcium hydroxide. Using this fact, a simple line-scan from the centroid location in each direction will produce an intensity curve with a distinctive peak at calcium/background transition. An example of the intensity profile is shown in Figure 22 below. After determining the size of the calcium area, the permeation distance was calculated as the difference in size from the t_0 scan to the current scan.

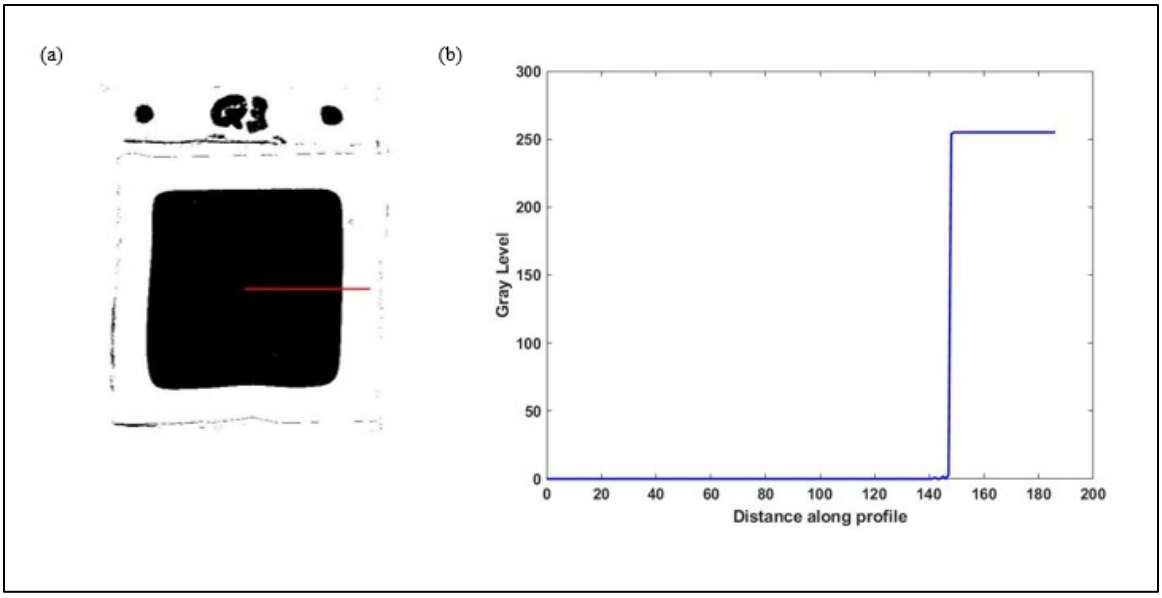

Figure 22: A calcium sample (a) with indicated intensity profile (b).

This peak was detected in the sub-routine, and its location was used to calculate the calcium degradation distance. For each sample, at least 4 measurements were taken per side. Additionally, sides would be eliminated from inspection if it was found that defects or other imperfections, like bubbles, caused irregularities in the degradation.

2.3.5 Moisture Ingress Rates

The movement of moisture through a polymeric material is described by the diffusivity and the concentration, as shown in Equation 3 below.

$$\frac{\partial C}{\partial t} = \nabla(D\nabla C) \tag{3}$$

For constant temperature experiments, the time scale of a one-dimensional diffusion controlled system will scale as the square of the characteristic distance *X*, such that

$$X = K\sqrt{t} \tag{4}$$

where K is a proportionality constant. This relationship is expected to hold for both Fickian and non-Fickian materials [31, 56, 57].

Figure 26 below shows the moisture ingress distance from the edge of the polymer as a function of time. As described previously, the ingress distance is the average of the 4 sides of the sample with at least 4 measurements taken per side, and sides were eliminated during the experiment if bubbles or other defects interfered with accurate measurement; this usually occurred during longer exposures. During long exposures with large ingress distances, it also became important to restrict the measurements to the center of each side. This preserves the one-dimensional nature of the ingress by eliminating areas where the calcium degradation became more "rounded". Straight line fits to Equation 4 were obtained for each material and the proportionality constants are listed with Figure 26. Since the data is plotted on a log-log scale, the slopes of the fits are all the same and reflect the proportional relationship of permeation distance X to $t^{0.5}$; the proportionality constant, K, is the y-intercept of the fitted lines.

The PDMS based materials (Corning, Qsil, HB Fuller) each exhibited the most rapid moisture ingress with K values of 0.92, 0.65, and 0.57, respectively. These materials were fully degraded in less than 10 hours at 85°C/85%RH. The results for the PDMS based encapsulant materials are shown in Figure 23 below.

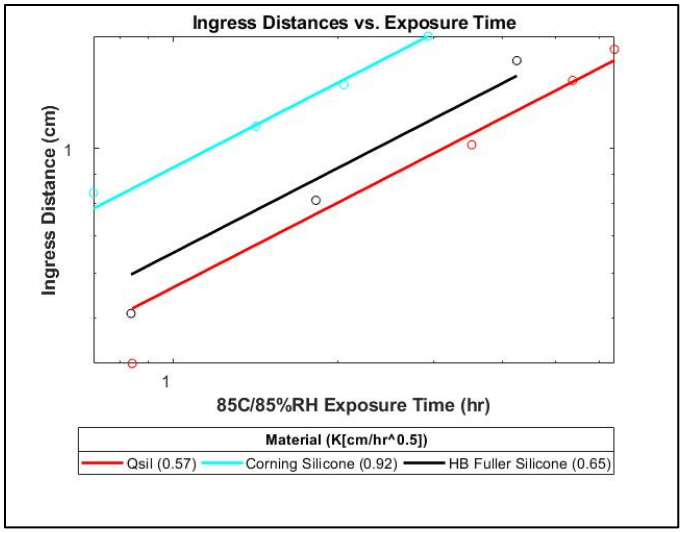

Figure 23: Permeation results for PDMS based encapsulants.

The EVA co-polymer performed slightly better with a *K* value of 0.36, and the ionomer (PV5400) performed better with a *K* value of 0.17. The results for the EVA and the ionomer are shown in Figure 24 below.

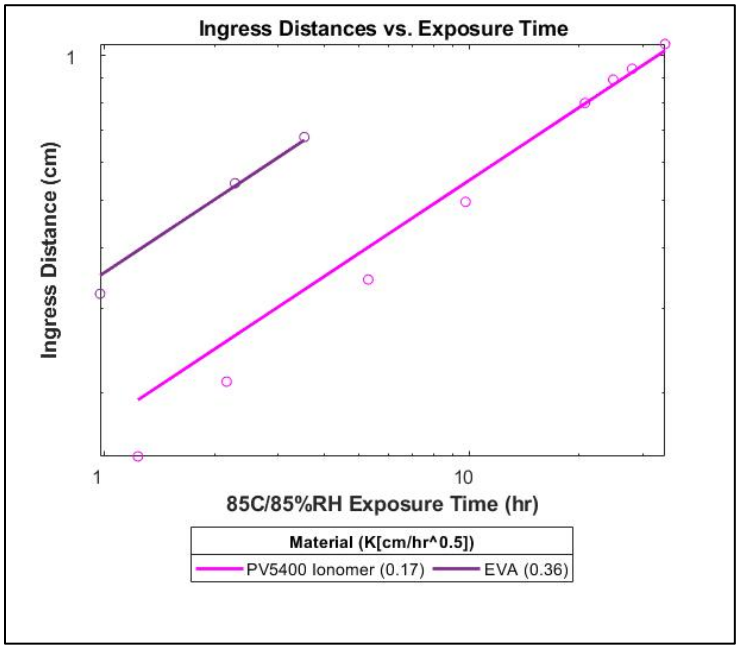

Figure 24: Permeation results for EVA and PV5400 ionomer encapsulants.

Both transparent PIB blends performed in a similar way with *K* values of 0.13 and 0.14, respectively. The transparent PIB blends displayed significant deviation from the

straight line fit over the course of the experiment, and this is attributed to significant bubbling present in the samples. While the fits to Equation 4 hold for Fickian and non-Fickian materials, the presence of bubbles causes a non-homogeneous permeation front and the accuracy of the fit suffers. The desiccant-filled PIB edge seal material (ADCO) exhibited the lowest diffusion rate with a K value of 0.013, which corresponds to approximately 1mm of ingress in 100 hours of exposure. It should be noted that the results for the 1:3 blend of transparent PIB and the ADCO material reflect a correction for edge-pinch, which is described in more detail in the following section. The results for the PIB based materials are shown in Figure 25, and the results for all materials under investigation are shown in Figure 26 below.

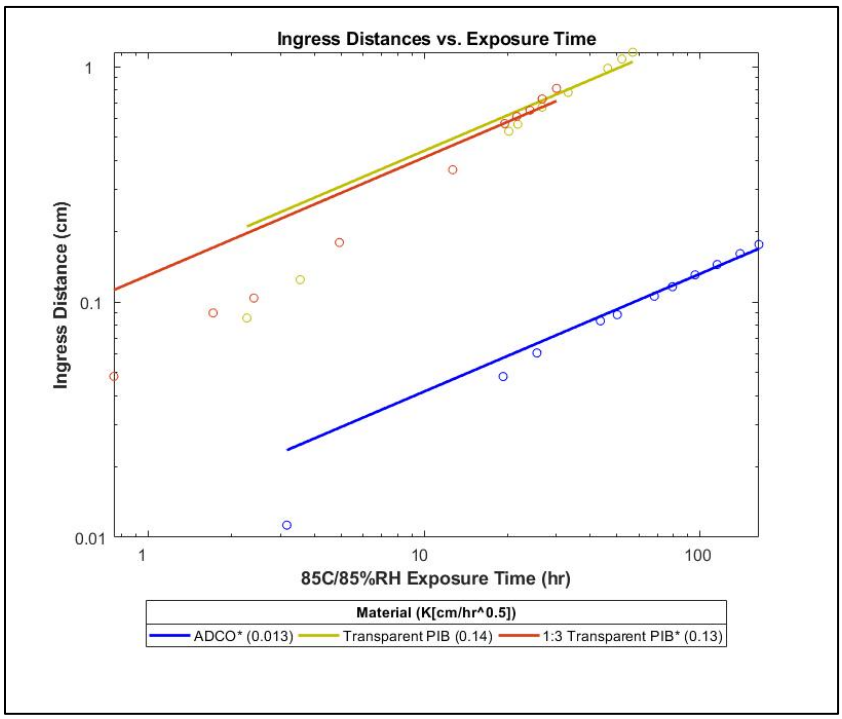

Figure 25: Permeation results for PIB based materials.

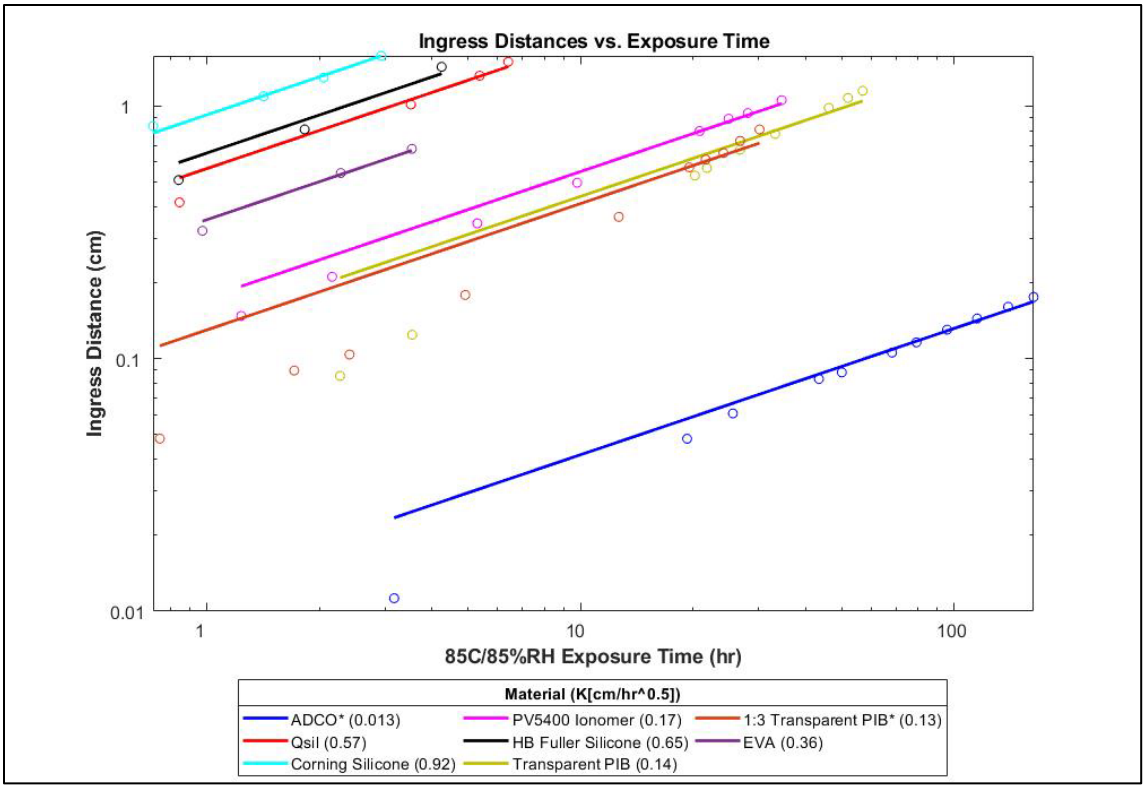

Figure 26: Moisture ingress distance as a function of 85°C/85%RH exposure time.

2.3.6 Edge Pinch in Optical Calcium Samples

It has been noted in previous work that the lamination of encapsulant and edge seal materials between glass substrates can yield a phenomenon called edge pinch, which is illustrated in Figure 27 below.

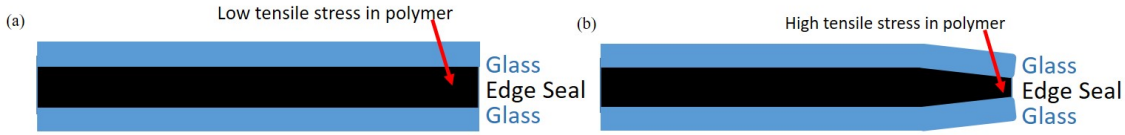

Figure 27: An example of (a) a properly laminated sample and (b) a sample with edge pinch.

When this occurs, the glass can be significantly bent at the edge, which reduces the thickness and increases the tensile stress in the polymer both of which affect moisture permeation [31, 58]. In this work, significant deviation from the straight-line fits to

Equation 4 was present for the ADCO polyisobutylene edge seal as well as the 1:3 blend of transparent polyisobutylene. In Figure 28 below, the original, unmodified, data is shown alongside the "corrected" data.

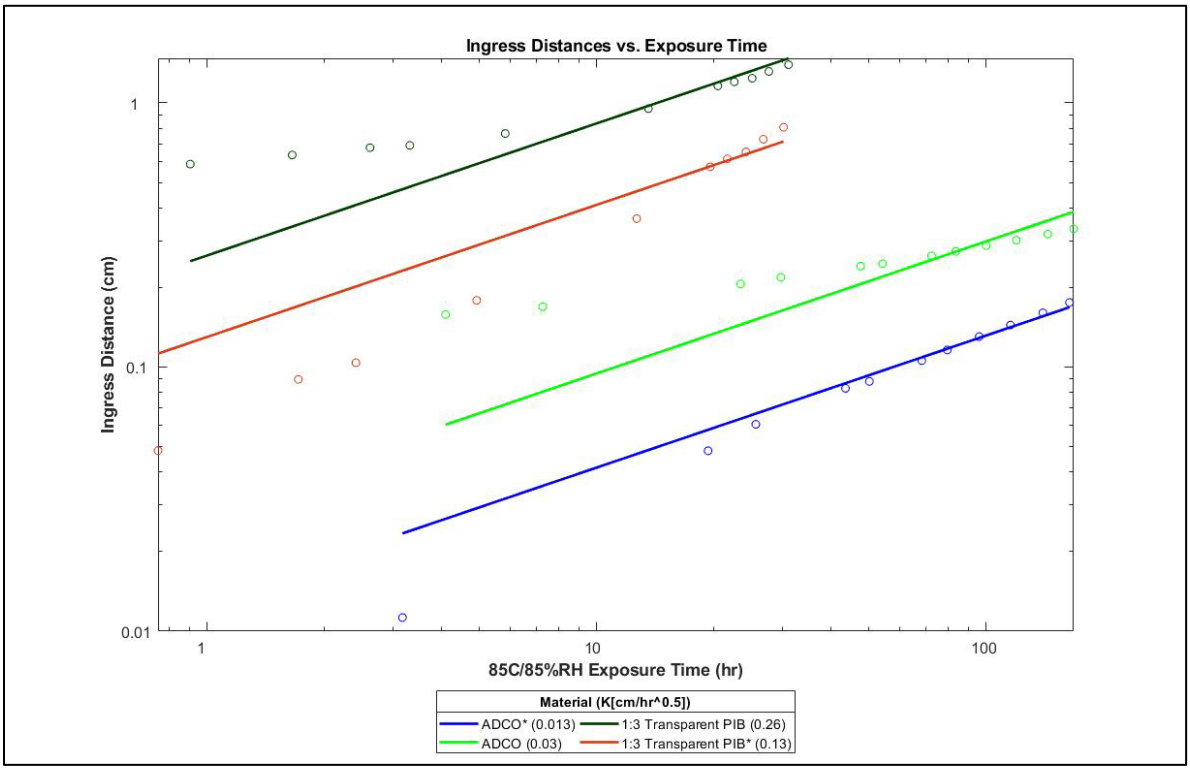

Figure 28: Permeation data for materials exhibiting edge pinch behavior.

The original *K* values for the 1:3 transparent PIB blend and ADCO are 0.26 and 0.03 respectively. From the data shown in Figure 28, the measured permeation distance for the first few measurements is higher than would be expected from the fits, which indicates that the edge of the materials is compromised. To account for this, a simple normalization was performed for the data in which the first measurement was subtracted from all subsequent measurements. After making this correction, the permeation constants for the 1:3 transparent PIB and ADCO were 0.13 and 0.013 respectively; the data also more closely matches the straight-line fits. Some deviation from the fits is still present, especially for the

transparent PIB, but this can be attributed to the significant number of bubbles present in the material noted previously.

2.4 Conclusion

The results of the optical calcium moisture ingress experiments provide further validation of the experiment as a method of evaluation the barrier performance of a wide range of encapsulant and edge seal materials. While the time scales under investigation in this work are limited, this experiment can be easily performed at large time scales for low-diffusivity materials or more mild aging conditions. The development of an automated measurement system also dramatically reduces the effort required to perform this experiment. With this, tedious and by-hand, measurements can be replaced with a faster and more accurate system.

The material-level results of this work also provide important insight into the barrier performance of many commonly used, commercially available, PV materials. The ingress distance results clearly indicate that the common encapsulants (PDMS, ionomers, EVA) provide little in terms of moisture protection. On the other hand, the desiccant-filled PIB edge seal provides by far superior moisture protection. Since these materials must provide both environmental protection and mechanical support, it is clear that encapsulation materials can add more value to the PV system by providing robust mechanical performance, while moisture protection is the domain of the edge seal. However, this conclusion does not diminish the importance of the mechanical properties of the edge seal. This work indicates that if the edge seal were to become mechanically decoupled, by delamination or other failure, from a PV system, then the device would be exposed to

moisture ingress. Therefore, the mechanical performance and integrity of the edge seal is of at least equal importance to that of the encapsulation materials; a conclusion that is supported by previous work [31]. Work performed in area of adhesion, along with various degradation studies, is described in the following chapter.

CHAPTER 3. MECHANICAL PERFORMANCE OF BARRIER MATERIALS

3.1 Introduction

Chapter 2 discussed the moisture barrier performance of many encapsulation and edge seal materials. It was found that, while the barrier performance of encapsulant materials is poor, their mechanical robustness is critical to device lifetime. For edge seals, the fact that they provide the only meaningful moisture protection highlights the importance of their mechanical integrity. Previous work has explored the mechanical properties of several encapsulant materials in rigid PV architectures, however little has been presented for flexible applications. In this chapter, the mechanical performance of several encapsulants and the desiccant-filled PIB edge seal is investigated. Particularly, the interfacial adhesion between these materials and a flexible, PET-based, front-sheet is studied. In this work, peel tests were used to study the adhesion strength of these materials. The peel test was selected primarily due to its simple test protocol, simple sample manufacturing, and applicability to flexible materials. Other methods exist for evaluating adhesion in terms of fracture energy, G_c [32, 34, 35, 37, 39], but attempts to adapt these methods to a wide range of flexible materials experienced repeatability issues and were low through-put. Therefore, these methods were abandoned in favor of the simpler peel test.

3.2 Experimental

3.2.1 Materials

In this work, several PET based substrates were used for peel test experiments. Baseline adhesion measurements and aging studies used MELINEX® ST505 (DuPont Teijin Films), which is a 125μm film that has been pre-treated on both sides for improved adhesion [59]. An investigation into the UV protection performance of the 3M Ultra Barrier solar film was also performed.

The adhesive materials selected for this work consisted of Qsil 216, a two-part polydimethylsiloxane formulation (Quantum Silicones); PHOTOCAP® 15580P, an ethylene vinyl acetate (EVA) copolymer available in a 0.46mm film (STR Solar); DuPont PV5400, an ionomer based encapsulant available in a 0.55mm film (DuPont); HelioSeal® 101 (commonly referred to as ADCO), a desiccant-filled polyisobutylene based sealant available in a 1cmx0.03cm tape (Royal Adhesives & Sealants). While the transparent PIB formulations performed well during the moisture permeation study, collaborators at NREL raised concerns about the long-term stability of this material. Based on these conversations the transparent PIB was eliminated from the mechanical evaluation portion of this work.

3.2.2 Peel Test Sample Fabrication

For all of the materials investigated in this work, the peel test specimen was a simple 3-layer laminate consisting of two substrate layers sandwiching the material of interest. Figure 29 illustrates the typical structure of a peel test specimen.

Figure 29: A typical peel test specimen consisting of substrates (blue) and adhesive (yellow).

3.2.2.1 Ethylene Vinyl Acetate Sample Fabrication

Several methods were used for manufacturing the peel test specimens depending on the manufacturer's specifications. The PHOTOCAP® EVA requires specific cure conditions that are detailed in the product documentation. The high pressure and temperature were achieved using a hot press (PHI Hydraulics) shown in Figure 30 below. The hot press consists two independently heated platens; the bottom platen being hydraulically actuated. The platens also contain a water cooling system which was used to cool samples after the cure cycle completed.

To manufacture peel specimens using the hot press, first the substrate and adhesive films were cut to approximately 8cm x 7cm pieces, and were cleaned with IPA. The pieces were then layered as shown in Figure 29. This laminate was then sandwiched on both sides by Teflon coated release liners, aluminum sheets, high-temperature resistant rubber sheets, and steel plates. The completed stack up, shown below in Figure 31 is then centered on the bottom platen of the hot press and heated.

(a) (b)

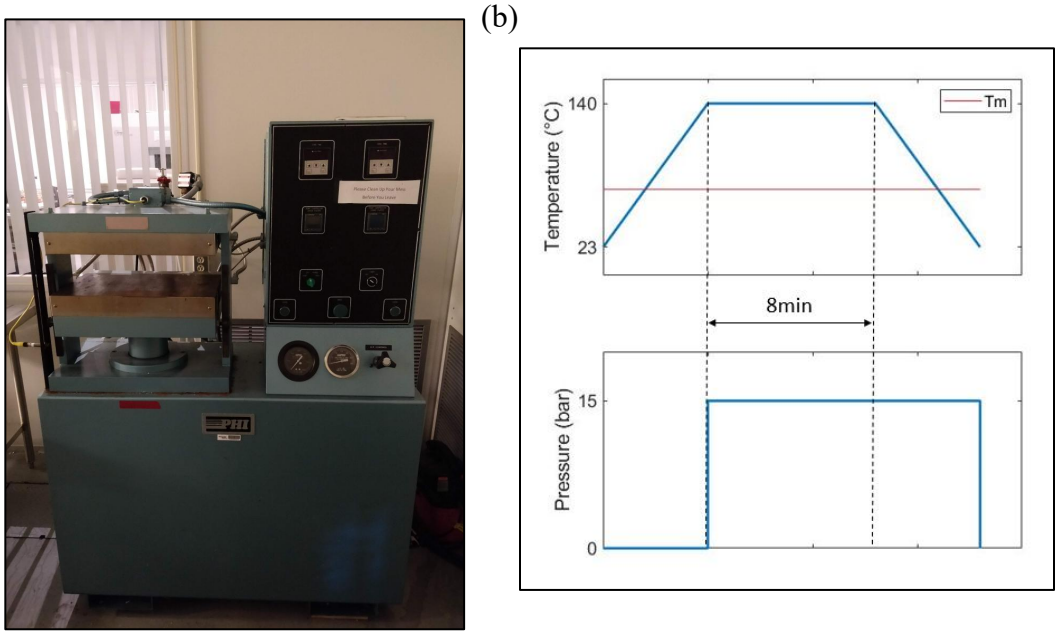

Figure 30: (a) Hot Press. (b) Temperature and Pressure Profiles.

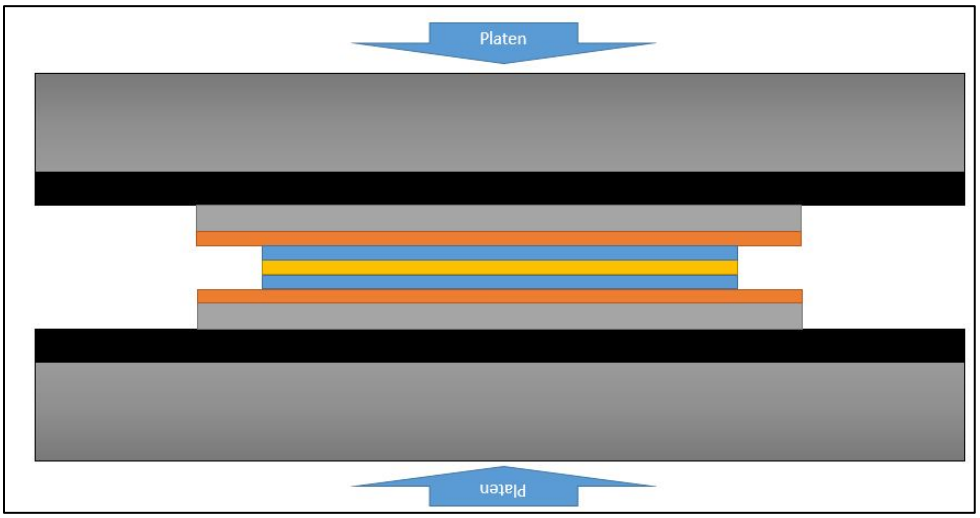

Figure 31: Stack up of materials for hot press lamination. The laminate of interest (blue/yellow/blue) is sandwiched symmetrically between PTFE release liners, aluminum sheets, rubber sheets, and steel plates.

The temperature and pressure profiles shown in Figure 30(b) are based on the requirements detailed in the product literature. Samples are heated on the open platens from

room temperature (~23°C) to the EVA curing temperature (140°C). Heating before lamination pressure is applied ensures the materials are at thermal equilibrium with the platens. Once heated, the platens are closed and held at a constant pressure of approximately 15bar. After the 8 minute cure cycle was completed, the samples were cooled using the platen cooling system. Samples were cooled until the indicated platen temperature was sufficiently below the melting point of the EVA formulation (~70°C); pressure was typically released around 35°C. Once cooled, the platens were separated, and the substrate/EVA laminate was removed and fully cooled to room temperature. A completed PET/EVA/PET laminate is shown in Figure 32 below. It should be noted that the lamination pressure used in this work is much higher than the value specified in the literature due to limitations of the press. However, it was found that high quality and defect free laminates were produced using the conditions described herein. Additionally, adhesion results detailed in subsequent sections confirm that good laminations were achieved.

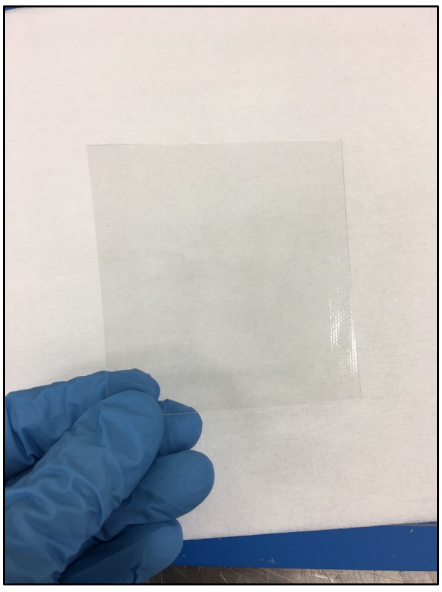

Figure 32: A completed EVA laminate.

3.2.2.2 PV5400 Ionomer Sample Fabrication

Similar to the EVA sample fabrication procedure, peel test samples using the PV5400 ionomer adhesive were made using the hot press. The lamination procedure for the ionomer was identical to the procedure for EVA, except the lamination pressure was applied for 1 hour. A completed PET/ionomer/PET laminate is shown in Figure 33 below.

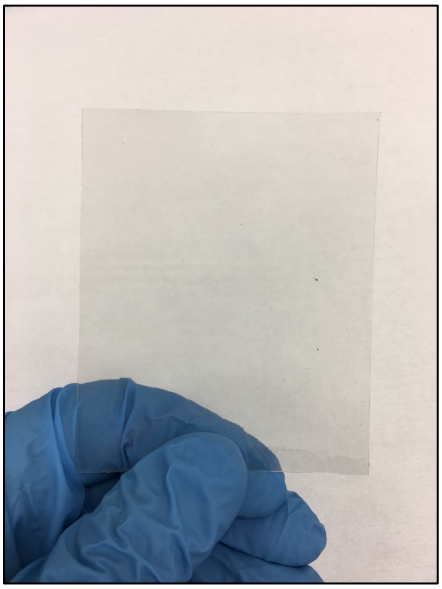

Figure 33: A completed PV5400 ionomer laminate.

3.2.2.3 Qsil 216 Sample Fabrication

The lamination procedure for the two-part PDMS formulation, Qsil 216, differs significantly from the procedure used for film and tape adhesives. Parts A and B were mixed in a 10:1 ratio in a clean container, and were de-aired in a vacuum chamber to remove bubbles trapped during the mixing process. During de-aeration, substrate materials were cleaned with IPA, and two strips of Kapton® tape were placed along the edges of one substrate. These tape strips act as dams for the uncured PDMS and help to keep the substrates parallel and separated at a distance of approximately 50µm. After the mixture

has been sufficiently de-aired, the Qsil mixture was deposited on the dammed substrate. After depositing an excess amount of Qsil, the second substrate is laminated on top using a rubber roller. The rolling motion is parallel to the Kapton® strips, which forces excess Qsil out of the stack-up. After lamination the uncured samples were transferred to a hot plate using a laboratory spatula, where they were thermally cured according to the manufacturer's specifications. A completed PET/Qsil/PET lamination is shown in Figure 34.

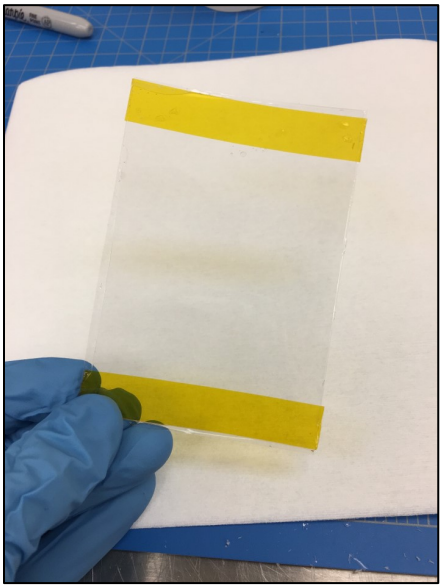

Figure 34: A completed Qsil laminate.

3.2.2.4 Polyisobutylene Sample Fabrication

The ADCO desiccant-filled PIB rubber used in this work was received from the manufacturer in tape form, and was stored in a dry N_2 glovebox to preserve its getter properties. Additionally, all peel test sample preparation with this material was conducted in the glovebox in order to ensure that moisture uptake was restricted to the aging studies. Outside the glovebox, substrate materials were cut into strips measuring roughly 20mm by

70mm, cleaned with IPA, and moved into the glovebox. Inside the glovebox, pairs of substrates were heated on a hotplate to 140°C. Then a strip of the PIB tape approximately 50mm long was adhered to one substrate followed by the second substrate; a hand roller was used to aid this step in the lamination process. After heating for approximately 15 seconds, the stack was quickly transferred to the pneumatic press described previously. The stack was then pressed and visually inspected to verify that no defects were present. After pressing, samples were allowed to cool and were stored in the glovebox until testing. A completed PIB peel test specimen is shown in Figure 35 below.

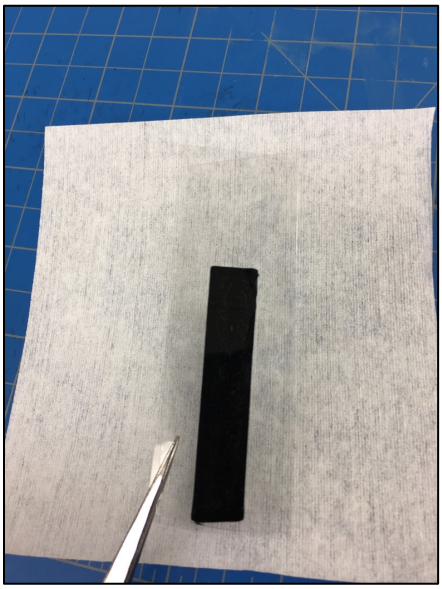

Figure 35: A completed ADCO PIB peel test laminate.

3.3 Adhesive Strength Measurement

After lamination of the peel test specimens using the procedures outlined above, individual peel test specimens were cut with a blade to 1cm strips. All peel testing described in this work was performed on a Universal Testing Machine (TestResources 100 Series, Figure 36(a)). The 100-series Universal Testing Machine (UTS) was fitted with

clamping jaws suitable for the flexible substrates under investigation, and either a 10N or a 1000N load cell was used depending on the expected adhesion strength. All peels were performed using displacement-controlled loading at 100mm/min, and the load-displacement data was automatically recorded throughout. Representative Load-Displacement plots shown in Figure 36(b) and Figure 36(c) depict some of the common behaviors present in the peel test data. Qsil and ADCO samples typically failed with load-displacement curves very similar to Figure 36(b), with an initial bump, followed by a consistent plateau. PV5400 and EVA samples typically produced curves similar to Figure 36(c). This type of failure, referred to as "stick-slip" is characterized by sharp saw-tooth peaks indicative of rapid and periodic, delamination. For both failure regimes, the peel strength was calculated as the average load over the displacement range in which the behavior is consistent. For materials with a plateau curve, the stable region could easily be programmatically determined using an error bound, but stick-slip behavior required manual assessment.

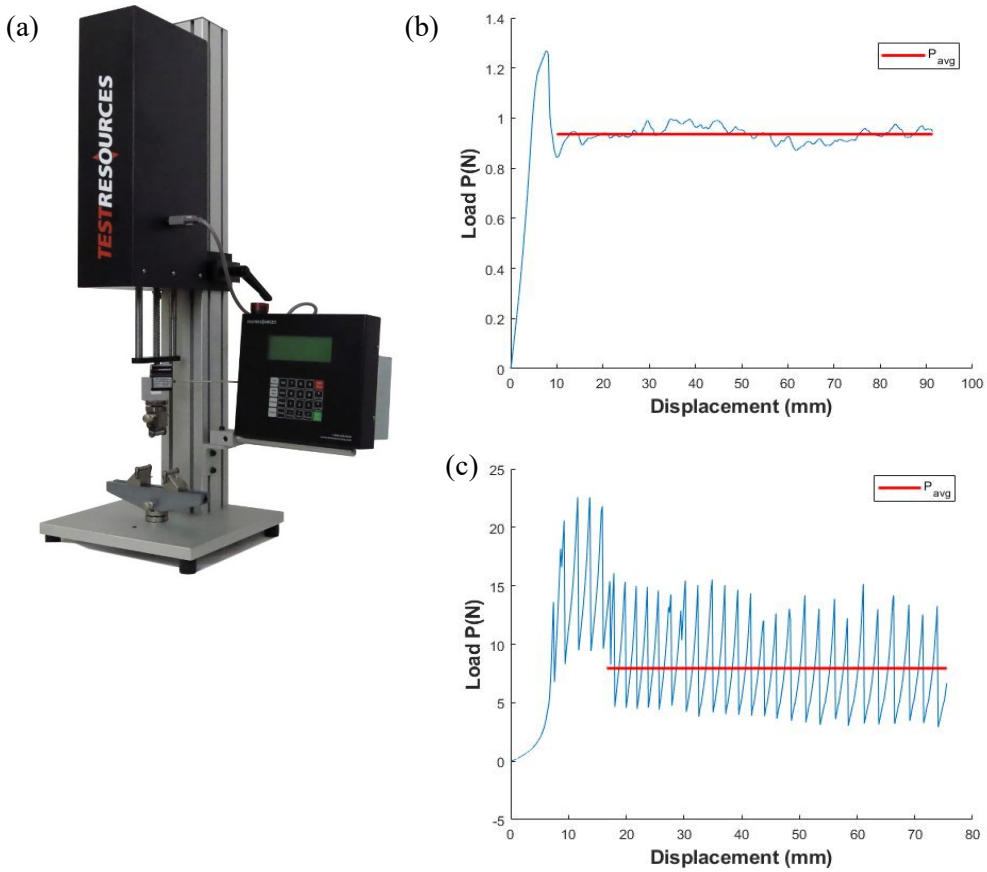

Figure 36: (a) The TestResources 100 Series Universal Testing Machine (www.testresources.net). (b) A typical load-displacement plot with a well-defined plateau. (c) A typical load-displacement plot with stick-slip behavior.

3.3.1 Initial Adhesion Strength

The initial adhesion strengths of Qsil, PV5400, EVA, and ADCO on ST505 PET substrates with no additional treatment are reported in Table 1 below; values have been normalized according to the 1cm width of all samples and are reported in N/mm. 5-8 samples were tested for each material. For the encapsulant materials, EVA exhibits by far the strongest adhesion to PET at ~1N/mm. The other encapsulant materials investigated, Qsil and PV5400 ionomer, both exhibited very poor adhesion at approximately 0.02N/mm. The edge seal material ADCO failed with an adhesion strength of 0.17N/mm.

Table 1: Initial Adhesion Strength on PET Substrates.

EVA	ADCO	Qsil	PV5400
1.015 ± 0.085	0.17 ± 0.045	0.022 ± .003	0.021 ± 0.002

From the initial adhesion results it is clear that EVA provides the most mechanical support in PET/Encapsulant/PET structures. The other encapsulant materials under investigation, Qsil and PV5400, both delaminated with extremely low strength, limiting their applicability without additional modification or treatment. The edge seal material, ADCO, performed better than Qsil or PV5400, but was approximately 17% as strong as the EVA. These results indicate that only EVA and ADCO exhibit sufficient strength to be of any practical use. Therefore, the aging studies described in this chapter will focus on these two materials.

3.3.2 Ultra-Violet Aging

Since PV materials in normal use will be exposed to UV radiation, the mechanical performance of the materials under investigation in this work subjected to UV exposure is of particular interest. Typical PV qualification standards, IEC 61215, 61646, and 61730-2 include a "UV Preconditioning Test" in which modules are exposed to 15kWhm^2 between 280 and 285nm at 60 ± 5°C [60]. In this work, peel test specimens are subjected to UV exposure and the effect on peel strength and failure mode is investigated.

3.3.2.1 Equipment

UV radiation was produced using a UV flood system (ELC-4001, Electro-Lite Corporation, Figure 37), which consists of a lamp rated for 125mW/cm^2 at 365nm, and a curing frame that positions the lamp at a controlled distance from the samples.

Figure 37: The ELC-4001 UV flood system (Electro-lite Corporation).

For the set-up used in this work, the power output of the lamp was measured using a thermopile to be 831W/m^2 at the sample surface. The incident UV spectrum was measured using a spectrometer (*Jaz*, Ocean Optics Inc.), and is shown in Figure 38 below.

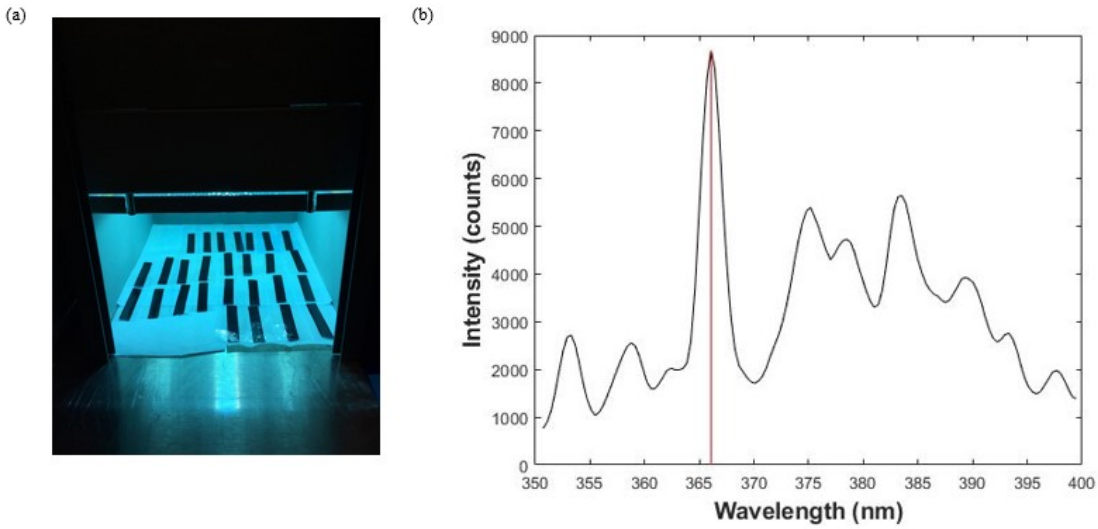

Figure 38: (a) Samples under UV treatment and (b) the incident UV spectrum.

3.3.2.2 EVA/PET UV Aging Results

Samples fabricated according to the procedures described previously were positioned under the UV lamp on a white backing material. Samples were removed periodically over the course of the experiment, cooled at room temperature for at least an hour, and tested for peel strength. The results for EVA/PET peel specimens aged under UV exposure are shown below in Figure 39; fitted splines are shown to guide the eyes, and 5-8 samples were tested for each data point. Error bars indicate the standard deviation of the peel strength. The results show an initial increase in adhesion strength up to about 1.7N/mm until approximately 1.9 MJ/m^2 of exposure, after which the adhesion strength rapidly declines and stabilizes at about 0.19 N/mm.

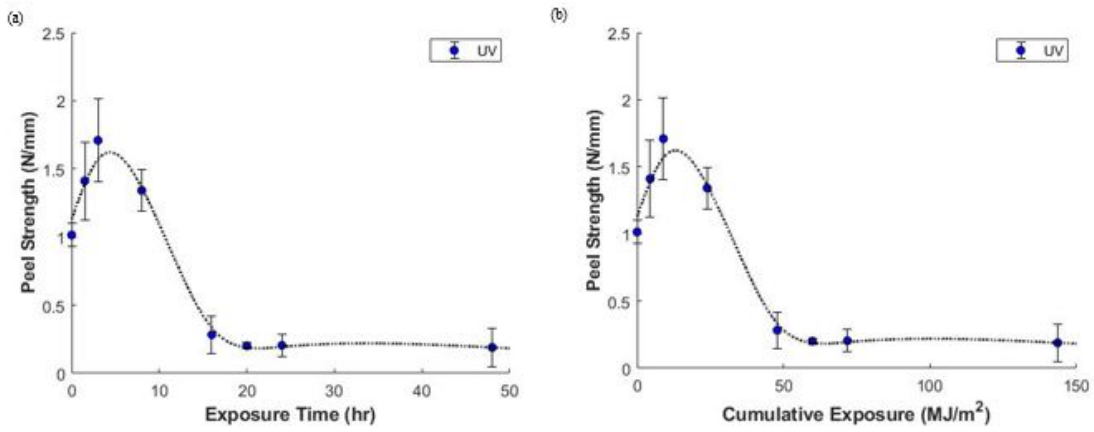

Figure 39: Peel strength versus UV exposure for PET/EVA peel specimens.

In addition to the change in peel strength, the mechanical behavior of the specimens changed dramatically during the experiment. While initial failure was characterized by stick-slip behavior, with periodic load peaks corresponding to rapid propagation of the delamination front, limited UV exposure up to about 24MJ/m^2 increased the amount of plateau-regime failure, resulting in cavitation bubbles on the delaminated EVA surface. Beyond 48 MJ/m^2 the adhesion strength decreased to approximately 19% of the original strength, and the delaminated EVA surface showed no visible signs of the cavitation behavior that was present at higher strengths. Optical microscope images of the delaminated EVA surface are shown in Figure 40, which illustrate these changes.

The temperature of the EVA/PET samples was also monitored during the UV aging experiment, and it was found that the samples reached a steady-state temperature of 65°C. In order to isolate possible effects of thermal degradation of the EVA/PET interface at this temperature, a separate thermal study of the EVA/PET peel strength was conducted and is described later.

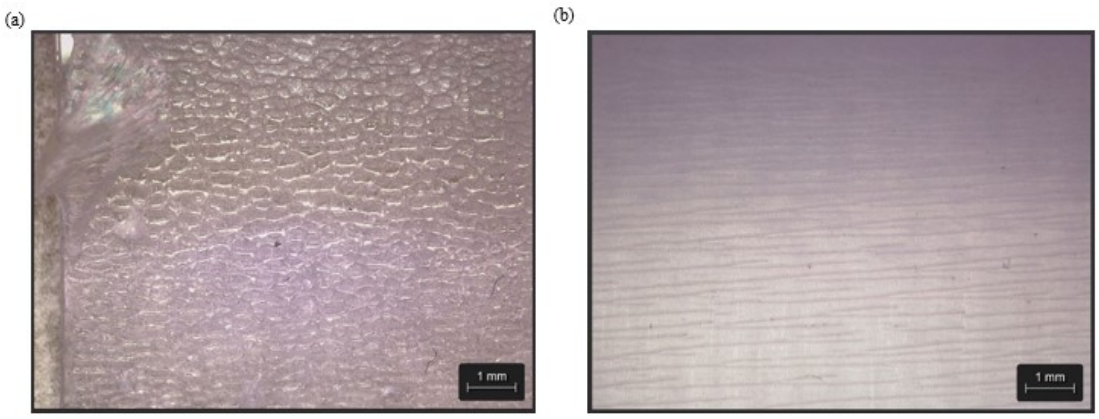

Figure 40: EVA delaminated surface with (a) cavitation bubbles and (b) without cavitation bubbles.

In addition the ST505 PET used for the bulk of the adhesion studies, some samples were also constructed using the 3M Ultra Barrier Film (UBF). This material, which is a multilayer laminate on a PET substrate, is also advertised as UV blocking at the wavelengths used for aging in this work. Several UBF/EVA/UBF peel samples were fabricated to investigate the effects of UV blockers, and the results are shown in below.

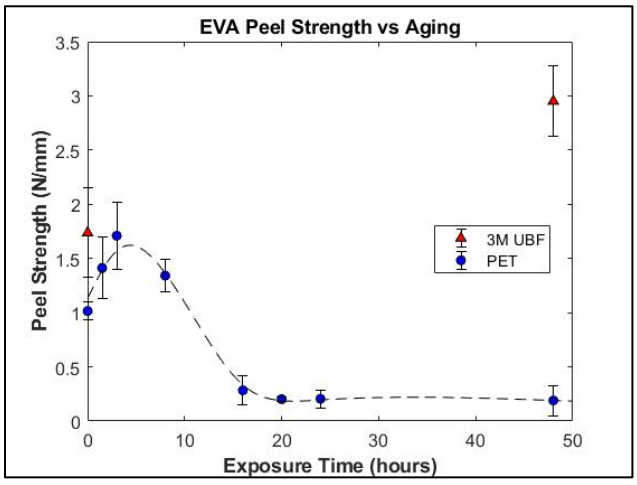

Figure 41: Peel strength versus UV exposure for EVA laminated to PET and 3M Ultra Barrier Film.

From the results it is clear that the 3M film had a protective effect on the EVA/3M UBF interface. It is not known if the same mechanisms causing increased strength in the

ST505 PET are also causing the strengthening in the 3M laminates, but the degrading effects of extended UV exposure seem to be mitigated, at least for the time scale of this study.

3.3.2.3 ADCO/PET UV Aging Results

Similar to EVA/PET peel samples, specimens constructed using the ADCO desiccant-filled polyisobutylene were aged under the UV flood system described previously. The changes in peel strength with respect to exposure time and cumulative UV dose are shown Figure 42 in below.

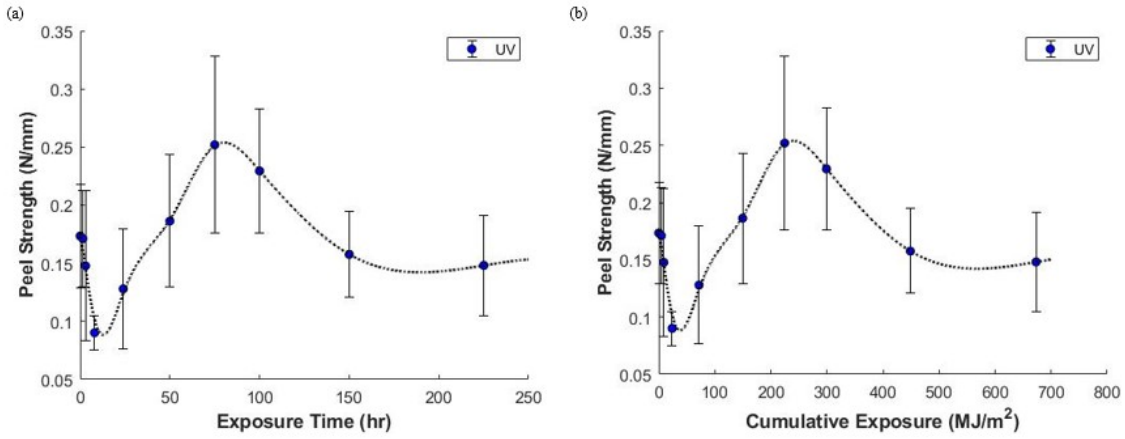

Figure 42: Peel strength versus UV exposure for PET/ADCO peel specimens.

The ADCO/PET peel strength behavior exhibited several distinct changes over the duration of the experiment. Initially the failure was predominantly adhesive, and very little cohesive residue was visible on the delaminated PET surface. Additionally, there was a rapid decrease in adhesion strength UV exposure up to approximately 38MJ/m^2. However, with continued exposure, adhesion strength steadily increased to a peak of about 0.25N/mm at 232MJ/m^2 of exposure; a 45% increase from the initial strength. Along with the

increased strength, the failure mode also changed from adhesive to cohesive, resulting in a visible layer of PIB residue on the delaminated PET surface. Optical microscope images illustrating this transition are shown in Figure 43 below.

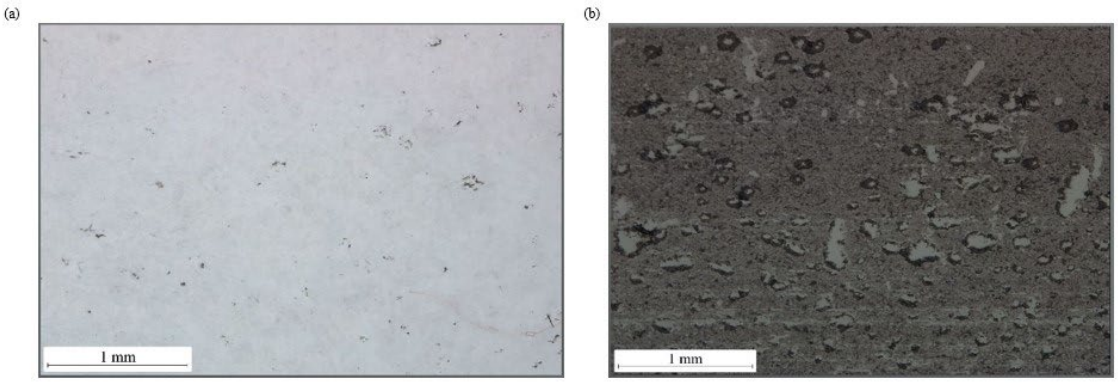

Figure 43: ADCO PIB delaminated surface with (a) adhesive failure and (b) cohesive failure.

However, the increased strength was not sustained with further UV exposure. Beyond 232MJ/m^2 of exposure the strength declined, while the failure mode remained cohesive. At the conclusion of the experiment, the peel strength was approximately 15% lower than the initial strength.

Similar to the EVA/PET samples, it was found that ADCO/PET peel samples were also heated during the UV exposure experiment. The surface temperature of the ADCO/PET samples was measured at 85°C and a separate thermal aging study at this temperature is described in the following section.

3.3.3 Thermal Aging

In order to isolate the UV aging from any collateral thermal effects, a set of EVA/PET and ADCO/PET peel specimens were aged in an oven at 65°C and 85°C

respectively, and the results are shown in Figure 44 below along with the UV aging results for comparison.

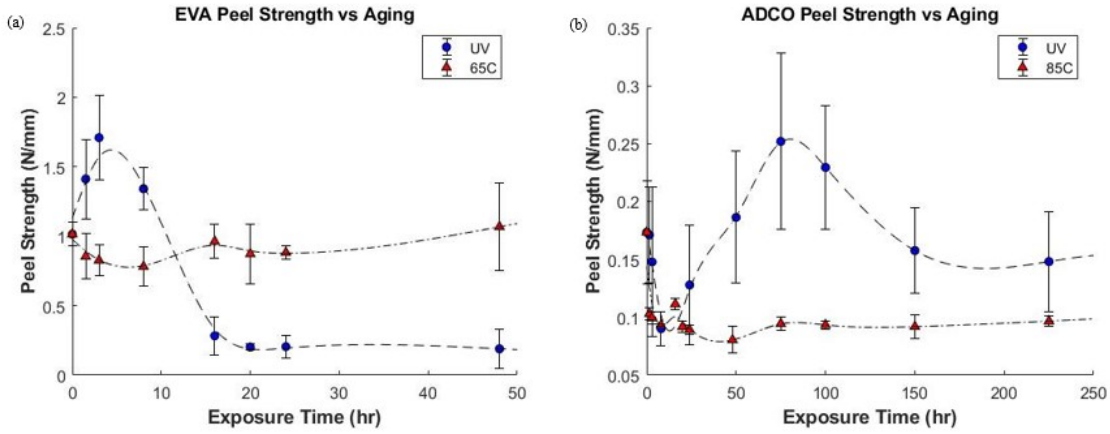

Figure 44: Peel strength vs exposure time for UV and thermal aging conditions of (a) EVA/PET and (b) ADCO/PET.

For the EVA/PET samples, the thermal aging results varied little compared to the more complex behavior of the UV aging results. The maximum change in peel strength for samples aged at 65°C occurred at 8 hours of exposure, where the strength decreased by approximately 23%. However, the strength recovered over time and at the 48 hour conclusion of the test the strength had increased by about 5% compared to the unaged specimens. Overall, the lack of a trend similar to the UV aged samples indicate that the phenomena present during UV exposure is independent of the thermal conditions.

For the ADCO/PET samples, the thermal aging results displayed similar behavior to the UV aging results for exposures up to about 8 hours. However, additional UV exposure resulted in the increase in strength and change in failure mode described previously, while additional thermal exposure had little effect. Additionally, the samples failed with predominantly adhesive behavior, with little cohesive reside that did not visibly

change with additional exposure. Therefore, it is likely that the initial decrease in strength for both aging conditions is a result of the increased temperature, but the subsequent strengthening seen in the UV study can be attributed to radiation effects. Further analysis of the peeled surfaces to investigate the underlying mechanisms is detailed later in this dissertation.

3.3.4 Damp Heat Aging

In addition to the UV and thermal aging studies, peel samples were also exposed 85°C/85%RH to investigate the effects of damp heat exposure on the adhesive interface between EVA encapsulant, ADCO PIB edge seal, and PET substrates. Samples were aged in the same environmental chamber described previously, and were removed periodically for testing. It has been noted in previous work that the amount of dry-out time after damp heat exposure has an effect on encapsulant peel strength [61]. In this work, those authors' recommendations were followed, and samples were peeled between 3 and 24 hours after removal from the chamber.

The results of the damp heat aging study are shown in Figure 45. The UV and thermal aging results are also included for ease of comparison. The EVA/PET peel samples were found to increase in peel strength and peaked at 16 hours of damp heat exposure. The increase in strength was also stable, with the peel strength staying between approximately 1.4-1.6N/mm; an increase of 40-60%. Samples also failed in the stick-slip regime for the duration of the damp heat experiment. The ADCO/PET samples aged under damp heat exposure behaved very similar to the thermally aged samples. The peel strength rapidly declined and stabilized after about 16 hours of exposure. Again the failure mode remained

predominantly adhesive, with very little cohesive residue that did not change visibly during the experiment.

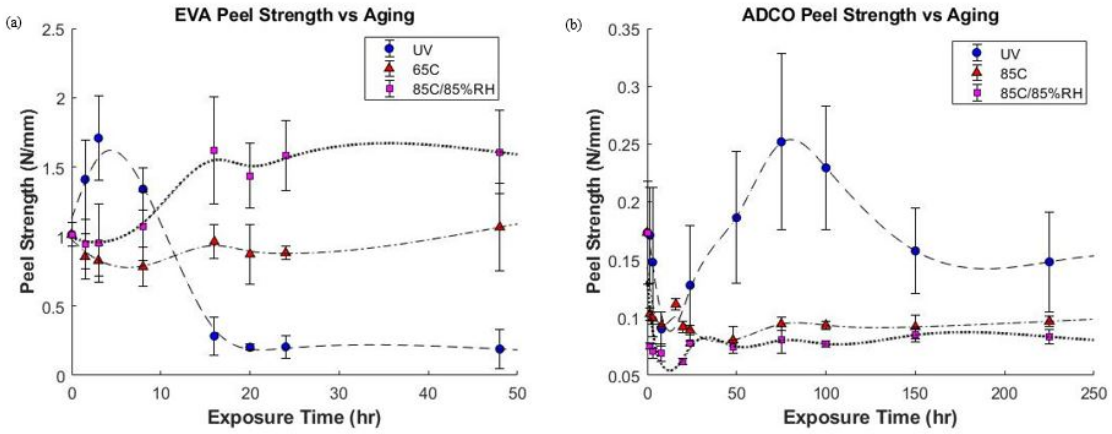

Figure 45: Complete aging results including UV, thermal, and damp heat studies for (a) EVA/PET and (b) ADCO/PET.

The damp heat aging appears to have had a beneficial effect on the peel strength of EVA/PET laminates, at least during the time scales under investigation in this work. However, it is likely that with enough exposure the peel strength, or other structural changes in the material would occur. Additionally, it appears from these results that a similar mechanism is affecting the ADCO/PET samples aged under elevated temperature and damp heat conditions, which makes intuitive sense give that both conditions are at the same temperature. In order to understand the chemical changes that are occurring at the interface further analysis was performed, and the details are described in the following section.

3.4 Surface Analysis

While peel strength measurement provides insight into the changes in behavior that encapsulant and edge seal material undergo during aging, the method does not provide any

information concerning the underlying mechanisms. Therefore, chemical surface characterization was conducting on the delaminated surface to investigate the changes that occurred at the interface. Much of the work described in this section was performed in collaboration with Jinho Hah of the C.P. Wong group at The Georgia Institute of Technology.

3.4.1 X-ray Photoelectron Spectroscopy

In order to investigate the chemical compositions of delaminated interfaces, X-ray photoelectron spectroscopy (XPS) was used. Samples were placed in a high vacuum environment and were irradiated with a focused beam of X-rays, which resulted in the emission of photoelectrons from the sample, as illustrated in Figure 46. These photoelectrons were then detected by the analyser, and their kinetic energy was measured by a spectrometer. The binding energy (E_b) of the surface electrons was then determined with Equation 5 using the known energy of the incident X-ray photons (hv), the kinetic energy of the emitted photoelectron (E_k), and the work function of the spectrometer (WF).

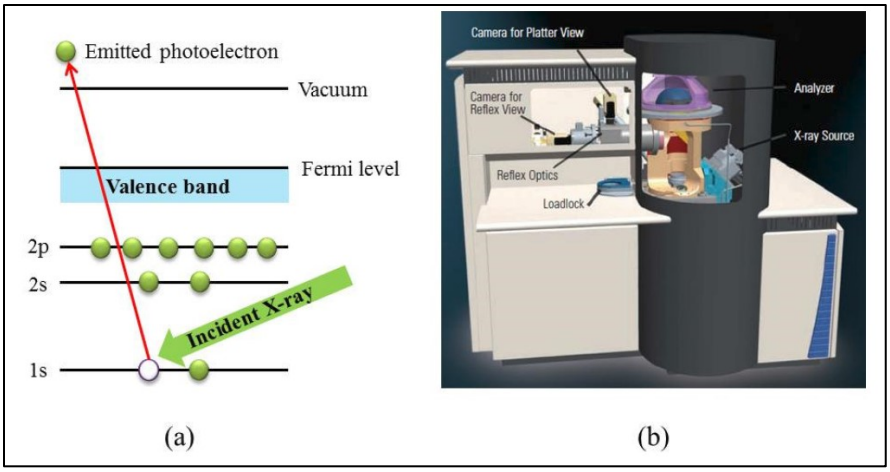

Figure 46: (a) The fundamental principle of photoelectron emission and (b) a Thermo Scientific XPS system similar to the one used in the work [33].

$$E_b = hv - E_k - WF \tag{5}$$

In this work, a K-alpha XPS system (Thermo Scientific) was used for the chemical analysis of delaminated surfaces. Al K-alpha X-ray radiation (1486.3 eV) was used as an excitation source, and the spot size was set to 400µm. Also, a flood gun was used to compensate the binding energy shift caused by charge condensation.

The results of the experiments were analysed using a commercial analysis suite (Avantage Data System, Thermo Scientific). For all of the analysis conducted in this work, the core elemental peaks were fitted to Lorrentz-Gaussian peaks. Additionally, the spectra were calibrated to ensure consistency to the first scan [33].

3.4.2 Ultra-Violet Aging Interfaces

In order to understand the chemical changes at the interface, XPS analysis was performed on the PET side of delaminated peel specimens; the peel strength data was reported previously in Figure 39 and Figure 42.

3.4.2.1 PET/EVA UV Analysis

Table 2 summarizes the survey spectra results of PET/EVA samples aged for 1.5 and 24 hours of UV exposure, as well as t_0 values for comparison. The reported results are the average of 5 points on the PET surface of each sample. From the results, C 1s, O 1s, and Si 2p peaks were present in all samples, while the N 1s peak was only identified at t_0 and in the 1.5 hour samples. In addition, the N 1s peak was also not detected on the EVA side. Therefore, it is hypothesized that the most probable bond cleavage site for the 24 hour UV aged samples is at the C-Si bond associated with the R' radicals, as shown in Figure 47 below.

Table 2: The average elemental composition of PET surfaces from UV aged EVA/PET samples. In collaboration with J. Hah [62].

		t_0	$t_{1.5}$	t_{24}
Element (%)	**C 1s**	73.97 ± 0.92	75.07 ± 0.54	74.01 ± 0.17
	O 1s	22.37 ± 0.95	21.39 ± 0.39	25.06 ± 0.19
	Si 2p	1.31 ± 0.19	1.32 ± 0.14	0.94 ± 0.19
	N 1s	2.35 ± 0.15	2.21 ± 0.15	Undetected
	O/C Ratio	0.30	0.28	0.34

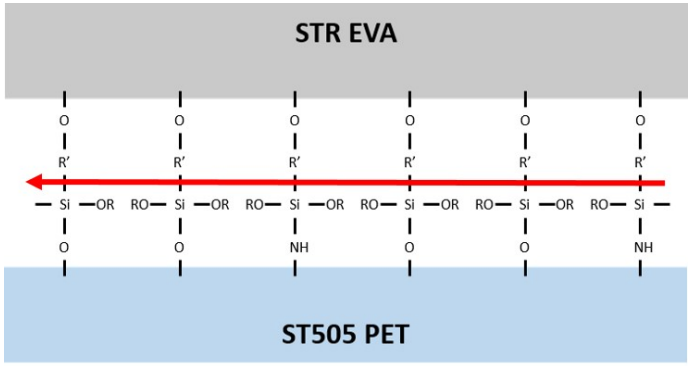

Figure 47: The bond cleavage path (red arrow) for EVA/PET exposed to UV for 24 hours. Note that –OR represents –(OCH_3) and –R'– represents –$CH_2CH(CH_3)CO_2(CH_2)_3$)– groups. Adapted from [62].

As described previously, adhesion strength increased with 1.5 hours of UV exposure, which corresponded to a decrease in the Oxygen/Carbon (O/C) ratio from 0.30

to 0.28 over the same time. Usually, UV radiation on PET increases the O/C ratio, as reported by Uchida *et al.* In their work it was found that 2 hours of UV exposure was sufficient to oxidize the PET surface to saturation [63]. In the case of the EVA/PET laminates investigated here, the observed decrease in O/C ratio is likely due to photopolymerization. While it is known that the PET is oxidized by UV radiation, the oxygen at the surface can be consumed by polymer radicals formed in the EVA by UV radiation [64]. Figure 48 illustrates the competing reaction between polymerization and oxidation present at the EVA/PET interface.

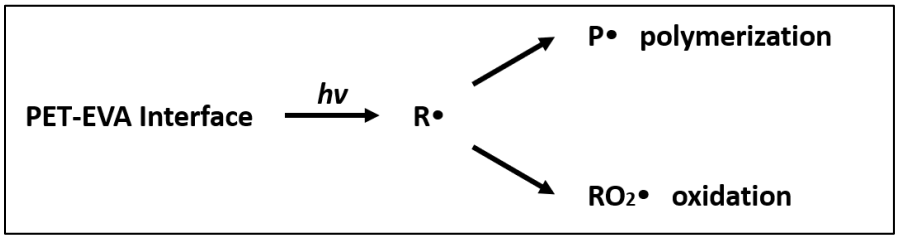

Figure 48: Pathways for UV driven polymerization and oxidation at the PET/EVA interface [64].

For 24 hour UV aged samples, a higher O/C ratio of 0.34 was observed, and a corresponding decrease in adhesion strength. This suggests that the UV-induced oxidation reaction dominated, overwhelming the photopolymerization reaction. Additionally, changes in the bulk EVA polymer could have an effect on the adhesive performance. For example, work by Jin *et al.* notes that mild UV exposure can increase crosslinking, which can improve mechanical properties like ultimate tensile stress and elongation at break [65].

3.4.2.2 PET/ADCO UV Analysis

Table 3 summarizes the detected elemental composition of the PET surface delaminated from PET/ADCO samples aged for 0, 8, 75, and 225 hours of UV exposure.

C 1s, O 1s, and Si 2p peaks were detected for all samples throughout the duration of the experiment, but N 1s was only detected for samples aged for 0 and 8 hours. Additionally, the deconvolution of the C 1s spectra is detailed in Table 4.

Table 3: The average elemental composition for PET surfaces delaminated from UV aged PET/ADCO specimens. In collaboration with J. Hah [62].

		t_0	t_8	t_{75}	t_{225}
Element (%)	**C 1s**	74.50 ± 0.51	73.24 ± 0.16	90.55 ± 0.52	90.03 ± 0.59
	O 1s	20.53 ± 0.30	20.38 ± 0.08	6.32 ± 0.43	6.34 ± 0.30
	Si 2p	3.27 ± 0.27	5.04 ± 0.10	3.13 ± 0.12	3.64 ± 0.30
	N 1s	1.70 ± 0.05	1.33 ± 0.09	Undetected	Undetected
O/C Ratio		0.28	0.28	0.07	0.07

Table 4: The average binding energies and full width half max (FWHM) of the C 1s spectra of UV Aged PET Surfaces from PET/ADCO samples. In collaboration with J. Hah [62].

			Components	Binding Energy (eV)	FWHM	Area (%)
t_0	**C 1s**	**A**	C-Si	283.0 ± 0.1	1.56 ± 0.02	1.07 ± 0.05
		B	C-C, C-H	285.0 ± 0.1	1.56 ± 0.02	73.55 ± 0.90
		C	C-O, C-NH*x*	286.7 ± 0.1	1.56 ± 0.02	14.43 ± 0.65
		D	NH*x*-C=O	287.6 ± 0.1	1.56 ± 0.02	0.60 ± 0.28
		E	O-C=O	289.1 ± 0.1	1.23 ± 0.03	10.35 ± 0.29
t_8	**C 1s**	**A**	C-Si	283.4 ± 0.1	1.60 ± 0.01	1.13 ± 0.17
		B	C-C, C-H	285.0 ± 0.1	1.60 ± 0.01	71.57 ± 0.57
		C	C-O, C-NH*x*	286.4 ± 0.1	1.60 ± 0.01	14.74 ± 0.13
		D	NH*x*-C=O	287.6 ± 0.3	1.60 ± 0.01	3.35 ± 0.38
		E	O-C=O	289.1 ± 0.1	1.19 ± 0.01	9.20 ± 0.13
t_{75}	**C 1s**	**A**	C-Si	283.3 ± 0.1	1.21 ± 0.01	2.52 ± 0.08
		B	C-C, C-H	285.0 ± 0.1	1.21 ± 0.01	93.15 ± 0.52
		C	C-O, C-NH*x*	286.4 ± 0.1	1.21 ± 0.01	2.85 ± 0.25
		D	NH*x*-C=O	287.6 ± 0.1	1.21 ± 0.01	0.82 ± 0.12
		E	O-C=O	289.1 ± 0.1	1.14 ± 0.01	0.65 ± 0.21
t_{225}	**C 1s**	**A**	C-Si	283.3 ± 0.1	1.24 ± 0.01	2.32 ± 0.07
		B	C-C, C-H	285.0 ± 0.1	1.24 ± 0.01	92.77 ± 0.65
		C	C-O, C-NH*x*	286.4 ± 0.1	1.24 ± 0.01	3.83 ± 0.59
		D	NH*x*-C=O	287.6 ± 0.1	1.24 ± 0.01	0.78 ± 0.12
		E	O-C=O	289.1 ± 0.1	1.09 ± 0.04	0.30 ± 0.05

As was seen in the peel strength results, the failure mode changed from adhesive to cohesive after 8 hours of UV exposure, and this is reflected in the XPS results. For bare PET, a survey spectra shows an N 1s peak, but this is not present for 75 hour and 225 hour UV aged samples with significant cohesive residue. Additionally, the O/C ratio decreases sharply for samples exposed for 75 hours and 225 hours, which corresponds to the presence

of ADCO residue (and its carbon black) on the delaminated surface. The cohesive strength changes seen in samples aged 75 hours and beyond can be attributed to changes in the bulk structure of the PIB polymer. Previous work on butyl rubber by Vinita *et al.* describes the chain scission reaction due to UV irradiation [66]. From Table 4, the proportion of C-C and C-H increases from ~72% to ~93%, which is evidence of chain scission in the PIB polymer backbone. Therefore, it is likely that the decrease in cohesive strength observed for samples aged with more than 75 hours of UV exposure is due to this process.

3.4.3 Thermal Aging of Interfaces

As described in Section 3.3.3, it was noted that samples became hot while under the UV lamp. In the case of the PET/EVA/PET samples the temperature during UV exposure was measured at 65°C, and the PET/ADCO/PET samples were measured at 85°C. This section details the results of XPS analysis of the delaminated PET surface from both materials.

3.4.3.1 PET/EVA Thermal Analysis

The peel strength of PET/EVA/PET samples aged at 65°C was reported previously in Figure 44. Compared to UV aging, the changes in behavior were far less pronounced for the thermally aged samples. Nonetheless, Table 5 summarizes the elemental composition of the delaminated PET surface of samples aged for 0, 8, 16, and 24 hours at 65°C. Again, the reported survey spectra are the average of 5 points on the surface.

Table 5: The average elemental composition of PET surfaces from EVA/PET samples aged at 65°C. In collaboration with J. Hah [62].

		t_0	t_8	t_{16}	t_{24}
Element (%)	**C 1s**	73.97 ± 0.92	68.96 ± 0.30	72.88 ± 0.62	73.53 ± 0.50
	O 1s	22.37 ± 0.95	24.61 ± 0.41	23.91 ± 0.68	23.66 ± 0.46
	Si 2p	1.31 ± 0.19	4.15 ± 0.31	0.71 ± 0.23	0.38 ± 0.18
	N 1s	2.35 ± 0.15	2.28 ± 0.24	2.51 ± 0.11	2.43 ± 0.11
O/C Ratio		0.30	0.36	0.33	0.32

C 1s, O 1s, Si 2p, and N 1s peaks were detected for all samples, and all aged samples exhibited an increased O/C ratio compared to t_0, which indicates that thermal oxidation has occurred. The samples aged for 8 hours had the highest O/C ratio and the lowest adhesion strength. The surface oxidation of PET and EVA is complex, but the oxidation of PET is known to facilitate the formation of terminal vinyl groups, phenols, and carboxylic acid end groups [67, 68]. Additionally, the deconvolution of the C 1s spectra detailed in Table 6 shows a continuous decrease in the area fraction of C-C, which is also indicative of surface oxidation of the PET. This is supported by similar observations in work from Gotoh *et al.* [69].

Table 6: Average binding energies, full-width-half-maxima, and area% of deconvoluted spectra from PET/EVA aged at 65°C. In collaboration with J. Hah [62].

			Components	Binding Energy (eV)	FWHM	Area (%)
t_0	C 1s	A	C-Si	283.0 ± 0.1	1.48 ± 0.02	1.17 ± 0.05
		B	C-C, C-H	285.0 ± 0.1	1.48 ± 0.02	66.29 ± 2.08
		C	C-O, C-NH*x*	286.6 ± 0.1	1.48 ± 0.02	17.09 ± 1.23
		D	NH*x*-C=O	287.7 ± 0.1	1.48 ± 0.02	2.12 ± 0.15
		E	O-C=O	288.9 ± 0.1	1.23 ± 0.01	13.34 ± 0.98
	O 1s	A	NH*x*-C=O	530.2 ± 0.1	1.55 ± 0.01	2.25 ± 0.63
		B	O=C-O	532.1 ± 0.1	1.55 ± 0.01	55.62 ± 1.07
		C	O-C=O	533.6 ± 0.1	1.55 ± 0.01	42.13 ± 1.67
	Si 2p	A	Si-C	100.2 ± 0.2	1.74 ± 0.06	1.27 ± 0.34
		B	Si-N	101.8 ± 0.1	1.74 ± 0.06	26.10 ± 3.13
		C	N-Si-O	102.6 ± 0.1	1.74 ± 0.06	49.10 ± 1.81
		D	Si-O	103.5 ± 0.1	1.74 ± 0.06	25.53 ± 2.52
t_8	C 1s	A	C-Si	283.1 ± 0.1	1.55 ± 0.02	1.40 ± 0.11
		B	C-C, C-H	285.0 ± 0.1	1.55 ± 0.02	65.76 ± 0.53
		C	C-O, C-NH*x*	286.6 ± 0.1	1.55 ± 0.02	17.86 ± 0.25
		D	NH*x*-C=O	288.0 ± 0.1	1.55 ± 0.02	0.84 ± 0.20
		E	O-C=O	288.9 ± 0.1	1.26 ± 0.01	14.15 ± 0.20
	O 1s	A	NH*x*-C=O	530.0 ± 0.1	1.54 ± 0.01	1.54 ± 0.04
		B	O=C-O	532.0 ± 0.1	1.54 ± 0.01	61.26 ± 0.30
		C	O-C=O	533.5 ± 0.1	1.54 ± 0.01	37.19 ± 0.29
	Si 2p	A	Si-C	99.6 ± 0.1	1.75 ± 0.06	1.22 ± 0.11
		B	Si-N	101.9 ± 0.1	1.75 ± 0.06	53.93 ± 1.66
		C	N-Si-O	102.7 ± 0.1	1.75 ± 0.06	43.04 ± 1.37
		D	Si-O	104.3 ± 0.2	1.75 ± 0.06	1.81 ± 0.34
t_{16}	C 1s	A	C-Si	283.0 ± 0.1	1.48 ± 0.03	1.20 ± 0.05
		B	C-C, C-H	285.0 ± 0.1	1.48 ± 0.03	63.21 ± 1.41
		C	C-O, C-NH*x*	286.6 ± 0.1	1.48 ± 0.03	18.51 ± 0.77
		D	NH*x*-C=O	287.8 ± 0.1	1.48 ± 0.03	2.35 ± 0.37
		E	O-C=O	288.9 ± 0.1	1.23 ± 0.02	14.73 ± 0.53
	O 1s	A	NH*x*-C=O	530.3 ± 0.2	1.53 ± 0.03	2.36 ± 0.59
		B	O=C-O	531.9 ± 0.1	1.53 ± 0.03	52.97 ± 0.93
		C	O-C=O	533.4 ± 0.1	1.53 ± 0.03	44.67 ± 0.55
	Si 2p	A	Si-C	100.0 ± 0.3	1.89 ± 0.09	2.36 ± 1.10
		B	Si-N	101.8 ± 0.1	1.89 ± 0.09	34.79 ± 1.31
		C	N-Si-O	103.2 ± 0.1	1.89 ± 0.09	55.82 ± 2.65
		D	Si-O	104.2 ± 0.2	1.89 ± 0.09	7.02 ± 3.83
t_{24}	C 1s	A	C-Si	283.0 ± 0.1	1.46 ± 0.01	1.17 ± 0.03
		B	C-C, C-H	285.0 ± 0.1	1.46 ± 0.01	63.49 ± 0.84
		C	C-O, C-NH*x*	286.6 ± 0.1	1.46 ± 0.01	18.61 ± 0.43
		D	NH*x*-C=O	287.8 ± 0.1	1.46 ± 0.01	1.94 ± 0.11
		E	O-C=O	288.8 ± 0.1	1.19 ± 0.01	14.79 ± 0.44
	O 1s	A	NH*x*-C=O	530.1 ± 0.1	1.50 ± 0.01	1.80 ± 0.06
		B	O=C-O	531.9 ± 0.1	1.50 ± 0.01	52.91 ± 0.21
		C	O-C=O	533.4 ± 0.1	1.50 ± 0.01	45.28 ± 0.24
	Si 2p	A	Si-C	99.9 ± 0.1	2.38 ± 0.11	1.59 ± 1.40
		B	Si-N	102.0 ± 0.2	2.38 ± 0.11	14.12 ± 8.26
		C	N-Si-O	102.9 ± 0.2	2.38 ± 0.11	78.95 ± 9.30
		D	Si-O	104.1 ± 0.2	2.38 ± 0.11	5.33 ± 2.11

From the XPS analysis of EVA/PET samples, there were observable changes occurring in the chemical state of the interface. However, a strong correlation to adhesion strength could not be found, so it is likely that 65°C is not hot enough to produce a dominating mechanism. This supports the conclusions from the UV aging study by eliminating the possibility of thermal effects.

3.4.3.2 PET/ADCO Thermal Analysis

The peel strength of PET/ADCO/PET samples was reported previously in Figure 44. These samples showed a sharp decrease in adhesion strength within a few hours of thermal aging, and did not exhibit the change in failure mode observed for UV aged samples. The survey spectra of the delaminated PET surfaces aged for 0, 8, 16, 50, and 225 hours is reported in Table 7 below.

Table 7: The average elemental composition of PET surfaces delaminated from PET/ADCO aged at 85°C. In collaboration with J. Hah [62].

		t_0	t_8	t_{16}	t_{50}	t_{225}
Element (%)	C 1s	74.50 ± 0.51	75.21 ± 0.51	76.41 ± 0.40	78.13 ± 1.05	78.40 ± 0.39
	O 1s	20.53 ± 0.30	19.20 ± 0.34	18.88 ± 0.47	17.13 ± 0.50	17.36 ± 0.47
	Si 2p	3.27 ± 0.27	4.26 ± 0.30	3.26 ± 0.15	3.32 ± 0.56	2.93 ± 0.12
	N 1s	1.70 ± 0.05	1.33 ± 0.09	1.45 ± 0.12	1.42 ± 0.10	1.31 ± 0.09
O/C Ratio		0.28	0.26	0.25	0.22	0.22

The most notable feature of the survey spectra is the decrease in the O/C ratio over the duration of the experiment. However, this is unexpected because thermal oxidation is the expected reaction at elevated temperatures [70]. This discrepancy is likely due to the presence of stabilizers in the ADCO PIB studied in this work. It is known that carbon black acts as a thermal antioxidant [71], so it is likely that this is the reason for the lack of observable oxidation. For further analysis, the deconvolution of the C 1s spectra is shown in Table 8.

Table 8: The average binding energies and full width half max (FWHM) of C 1s spectra of PET Surfaces of delaminated PET/ADCO specimens aged at 85 C. In collaboration with J. Hah [62].

			Components	Binding Energy (eV)	FWHM	Area (%)
		A	C-Si	283.0 ± 0.1	1.56 ± 0.02	1.07 ± 0.05
		B	C-C, C-H	285.0 ± 0.1	1.56 ± 0.02	73.55 ± 0.90
t_0	**C 1s**	**C**	C-O, C-NH*x*	286.7 ± 0.1	1.56 ± 0.02	14.43 ± 0.65
		D	NH*x*-C=O	287.6 ± 0.1	1.56 ± 0.02	0.60 ± 0.28
		E	O-C=O	289.1 ± 0.1	1.23 ± 0.03	10.35 ± 0.29
		A	C-Si	283.0 ± 0.1	1.57 ± 0.02	0.89 ± 0.10
		B	C-C, C-H	285.0 ± 0.1	1.57 ± 0.02	75.33 ± 0.47
t_8	**C 1s**	**C**	C-O, C-NH*x*	286.6 ± 0.1	1.57 ± 0.02	13.03 ± 0.27
		D	NH*x*-C=O	287.6 ± 0.1	1.57 ± 0.02	2.12 ± 0.15
		E	O-C=O	288.8 ± 0.5	1.19 ± 0.01	8.63 ± 0.19
		A	C-Si	283.1 ± 0.1	1.55 ± 0.03	1.23 ± 0.08
		B	C-C, C-H	285.0 ± 0.1	1.55 ± 0.03	73.83 ± 1.22
t_{16}	**C 1s**	**C**	C-O, C-NH*x*	286.3 ± 0.2	1.55 ± 0.03	13.55 ± 0.79
		D	NH*x*-C=O	287.6 ± 0.1	1.55 ± 0.03	2.50 ± 0.34
		E	O-C=O	289.1 ± 0.1	1.19 ± 0.01	8.88 ± 0.33
		A	C-Si	283.0 ± 0.1	1.52 ± 0.02	1.07 ± 0.08
		B	C-C, C-H	285.0 ± 0.1	1.52 ± 0.02	76.89 ± 0.39
t_{50}	**C 1s**	**C**	C-O, C-NH*x*	286.6 ± 0.1	1.52 ± 0.02	11.96 ± 0.31
		D	NH*x*-C=O	287.6 ± 0.1	1.52 ± 0.02	2.29 ± 0.17
		E	O-C=O	289.2 ± 0.1	1.19 ± 0.01	7.79 ± 0.31
		A	C-Si	283.0 ± 0.1	1.55 ± 0.04	1.10 ± 0.15
		B	C-C, C-H	285.0 ± 0.1	1.55 ± 0.04	76.40 ± 0.58
t_{225}	**C 1s**	**C**	C-O, C-NH*x*	286.6 ± 0.1	1.55 ± 0.04	12.34 ± 0.49
		D	NH*x*-C=O	287.6 ± 0.1	1.55 ± 0.04	2.07 ± 0.22
		E	O-C=O	289.2 ± 0.1	1.22 ± 0.01	8.09 ± 0.35

The deconvoluted data shows an increase in NH*x*-C=O content and a decrease in O-C=O content after 8 hours of 85°C exposure which corresponds to the observed decrease in adhesion strength. However, a distinct weakening mechanism cannot be conclusively determined due to scarce literature and a need for more in depth analysis.

3.4.4 Damp Heat Aging of Interfaces

Delaminated peel specimens subjected to damp heat aging at 85°C/85%RH were also analysed using XPS. The peel strength data reported in Figure 45 showed that, for EVA/PET, up to 16 hours of exposure increased peel strength, and additional exposure up

to 48 hours had no further effect. ADCO/PET showed a similar trend to the thermally aged samples, with a sharp initial decrease in strength and no further change.

3.4.4.1 PET/EVA Damp Heat Analysis

Table 9 summarizes the elemental peaks detected on the delaminated PET surface for samples aged in damp heat for 0, 1.5, 16, and 24 hours. These results were calculated from survey spectra and are the average of 5 points on the surface of each sample. C 1s, O 1s, Si 2p, and N 1s peaks were detected in all samples, and samples aged for 1.5 and 16 hours have lower O/C ratios. This suggests that free oxygen at the interface has been consumed, which was not seen for UV or thermally aged samples discussed previously.

Table 9: Average elemental composition of PET surfaces from EVA/PET samples aged at 85°C/85%RH. In collaboration with J. Hah. [62]

		t_0	$t_{1.5}$	t_{16}	t_{24}
Element (%)	**C 1s**	73.97 ± 0.92	75.70 ± 0.32	75.25 ± 0.45	75.23 ± 0.42
	O 1s	22.37 ± 0.95	20.36 ± 0.14	21.49 ± 0.33	22.25 ± 0.16
	Si 2p	1.31 ± 0.19	1.62 ± 0.51	0.60 ± 0.05	0.28 ± 0.16
	N 1s	2.35 ± 0.15	2.32 ± 0.15	2.67 ± 0.17	2.24 ± 0.21
O/C Ratio		0.30	0.27	0.29	0.30

After lamination, silane coupling agents in the EVA are bonded to hydroxyl (–OH) and amine ($–NH_2$) groups present on the PET, which is illustrated in Figure 49. However, damp heat exposure introduce H_2O, which causes alkoxy groups to undergo hydrolysis and form hydroxy groups. This reaction is described in Equation 6 below.

$$\text{PET-O-Si-}(OCH_3)_2\text{-R'-O-EVA} \rightleftharpoons \text{PET-O-Si-}(OH)_2\text{-R'-O-EVA} \quad (6)$$

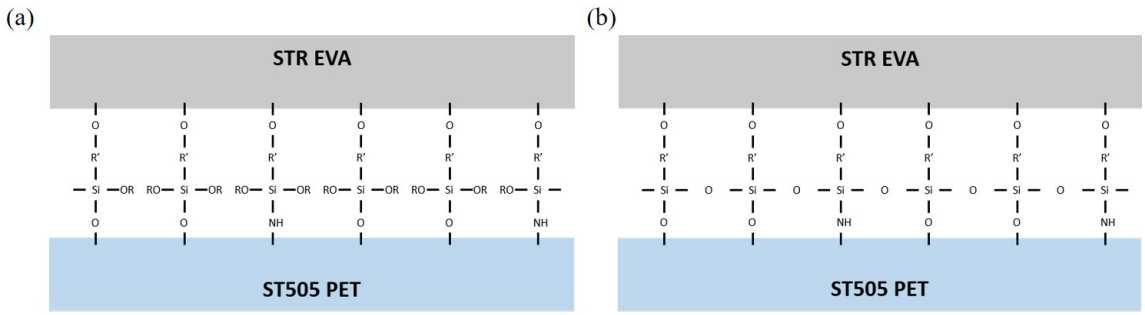

Figure 49: Schematic of PET-EVA interface (a) after lamination process and (b) after damp-heat exposure. Note that –OR represents –(OCH3) and –R'– represents –CH2CH(CH3)CO2(CH2)3)– groups. Adapted from [62].

The hydrolysis reaction forms a silanol group in the presence of water. However, there is also a reverse hydrolysis, i.e. condensation, reaction occurring to form a siloxane linkage (Si-O-Si) at the surface. This equilibrium reaction in described in Equation 7 [28].

$$\text{HO-Si-OH} + \text{HO-Si-OH} \rightleftharpoons \text{H}_2\text{O} + \text{Si-O-Si} \tag{7}$$

Therefore, it is expected that the concentration of siloxane linkages would increase as illustrated in Figure 49(b), and the increase in adhesion strength can be attributed to the increase in crosslinking due to formation of this strong Si-O-Si network. Similar conclusions were drawn in work by Jin *et al*., in which mild increases in crosslinking were shown to increase tensile strength and elongation at break [65]. Modest increases in these mechanical properties would result in more compliant behavior in the EVA, which in turn would increase the load required to delaminate it from PET.

3.4.4.2 PET/ADCO Damp Heat Analysis

Table 10 shows the elemental compositions present on delaminated PET surfaces from PET/ADCO samples aged under damp heat conditions for 0, 8, 16, and 24 hours. C 1s, O 1s, Si 2p, and N 1s were present in all samples, and the O/C ratio remained relatively

constant throughout the experiment. Similar to the samples aged at 85°C, thermal oxidation at the elevated temperature condition is an expected reaction, and the lack of significant changes in the O/C data is likely due to stabilizers.

Table 10: The average elemental composition from survey spectra of PET surfaces from PET/ADCO samples aged in damp heat. In collaboration with J. Hah [62]

		t_0	t_8	t_{16}	t_{100}
Element (%)	**C 1s**	74.50 ± 0.51	72.78 ± 0.53	73.19 ± 0.22	73.87 ± 0.61
	O 1s	20.53 ± 0.30	20.39 ± 0.23	20.62 ± 0.23	21.27 ± 0.36
	Si 2p	3.27 ± 0.27	5.12 ± 0.43	4.35 ± 0.15	3.06 ± 0.24
	N 1s	1.70 ± 0.05	1.71 ± 0.09	1.85 ± 0.13	1.81 ± 0.09
O/C Ratio		0.28	0.28	0.28	0.29

Additionally, the deconvolution of the C 1s spectra, detailed in Table 11 below, shows an increase in the C-Si component throughout this experiment. Similar to the EVA/PET samples aged in damp heat, this is evidence of a hydrolysis and condensation reactions involving the (–OH) groups present on the PET. However, more work is needed to fully understand the results and their relation to the observed weakening of the interface.

Table 11: The average binding energies and full width half maxima (FWHM) of the C 1s spectra of PET surfaces delaminated from ADCO/PET samples aged under damp heat. In collaboration with J. Hah [62].

			Components	Binding Energy (eV)	FWHM	Area (%)
t_0	C 1s	**A**	C-Si	283.0 ± 0.1	1.56 ± 0.02	1.07 ± 0.05
		B	C-C, C-H	285.0 ± 0.1	1.56 ± 0.02	73.55 ± 0.90
		C	C-O, C-NH*x*	286.7 ± 0.1	1.56 ± 0.02	14.43 ± 0.65
		D	NH*x*-C=O	287.6 ± 0.1	1.56 ± 0.02	0.60 ± 0.28
		E	O-C=O	289.1 ± 0.1	1.23 ± 0.03	10.35 ± 0.29
t_8	C 1s	**A**	C-Si	283.2 ± 0.1	1.60 ± 0.01	1.23 ± 0.19
		B	C-C, C-H	285.0 ± 0.1	1.60 ± 0.01	71.70 ± 1.15
		C	C-O, C-NH*x*	286.6 ± 0.1	1.60 ± 0.01	14.36 ± 0.48
		D	NH*x*-C=O	287.6 ± 0.1	1.60 ± 0.01	3.11 ± 0.40
		E	O-C=O	289.2 ± 0.1	1.20 ± 0.01	9.59 ± 0.14
t_{16}	C 1s	**A**	C-Si	283.1 ± 0.1	1.59 ± 0.01	1.32 ± 0.18
		B	C-C, C-H	285.0 ± 0.1	1.59 ± 0.01	71.32 ± 0.73
		C	C-O, C-NH*x*	286.6 ± 0.1	1.59 ± 0.01	14.56 ± 0.44
		D	NH*x*-C=O	287.6 ± 0.1	1.59 ± 0.01	2.29 ± 0.18
		E	O-C=O	289.1 ± 0.1	1.20 ± 0.01	10.51 ± 0.22
t_{100}	C 1s	**A**	C-Si	283.1 ± 0.1	1.59 ± 0.01	1.49 ± 0.18
		B	C-C, C-H	285.0 ± 0.1	1.59 ± 0.01	69.19 ± 0.44
		C	C-O, C-NH*x*	286.6 ± 0.1	1.59 ± 0.01	15.78 ± 0.23
		D	NH*x*-C=O	287.7 ± 0.1	1.59 ± 0.01	1.50 ± 0.42
		E	O-C=O	289.0 ± 0.1	1.22 ± 0.01	12.05 ± 0.28

3.5 Conclusion

The results of the mechanical characterization have provided valuable insight into the performance and degradation several encapsulants, as well as an edge seal material. High performing materials were subsequently aged in several accelerated conditions to simulate environmental exposure, and the changes in peel strength performance were evaluated. Chemical analysis of the delaminated samples using XPS was also conducted to further investigate the fundamental mechanisms that affect adhesion.

From initial, unaged, peel strength measurements, EVA has the best peel strength of the investigated encapsulant materials, while Qsil (PDMS) and PV5400 (ionomer) both perform poorly. The ADCO PIB-based edge seal material exhibited modest adhesion, which highlights the need to understand its long term performance because maintaining adhesion is critical for moisture protection. From these results, EVA and ADCO were selected for further aging studies and analysis to better evaluate their applicability for flexible PV packaging.

Ultra-violet aging of EVA bonded to PET produced complex behaviors. Some UV exposure improved the adhesion between EVA and PET, while extended exposure severely degraded the interface. Chemical analysis of this interface suggests a completion between a strengthening polymerization reaction and a weakening oxidation reaction. Therefore, the UV exposure of architectures using these materials must be limited. Additionally, it was found that the commercially available 3M Ultra Barrier Film, with its low transmittance at UV wavelengths provides good protection to the PET/EVA interface,

which exemplifies the important of using UV blocking layers in flexible top-sheet materials.

Ultra-Violet aging of ADCO bonded to PET also produced interesting behaviors. Initially UV exposure severely weakened the bond, but further exposure increased the strength until the failure mode transitioned from adhesive to cohesive. It is likely that the transition from adhesive to cohesive is due to photo oxidation of the interface. The changes in cohesive strength can be attributed to changes in the bulk properties of the PIB, and there is evidence of a chain scission reaction weakening the bulk structure of the polymer.

In order to isolate the effects of thermal exposure, peel samples constructed with EVA and ADCO were aged at the same temperature they experienced during UV exposure. The XPS results for EVA/PET aged at 65°C shows some evidence of thermal oxidation, but the lack of significant strength changes shows that the effects were minimal. Additionally, this confirms the previous UV results. ADCO/PET samples aged at 85°C experienced a rapid and substantial decrease in adhesion strength, which was sustained for the entire experiment. While thermal oxidation of the interface is likely, the presence of stabilizers in the PIB may be limiting the observable changes. Further analysis of this interface is needed to fully understand the mechanisms.

Finally, a study of the effects of damp heat exposure on adhesion strength of these materials was conducted. Interestingly, the EVA/PET interface increased in strength during the experiment. Chemical analysis of the interface provides evidence of hydrolysis and condensation reactions, which result in the formation of a strong Si-O-Si linkage at the interface. Since the experiment in this work was conducted for a relatively short time,

future work should investigate the long term behavior. ADCO/PET samples aged in damp heat were very similar to samples aged at elevated temperature, and again further experiments and analysis are needed to understand the fundamental mechanisms here.

To summarize, the mechanical performance of encapsulant and edge seal materials in flexible architectures was evaluated for a variety of aging conditions. The results and conclusions detailed herein provide useful guidance for material selection in flexible PV packaging, and also provide a foundation for further work in this area.

CHAPTER 4. CONCLUSION

The research detailed in this work has been conducted to investigate various aspects of flexible PV packaging. Since PV modules, especially thin-film varieties, are very sensitive to environmental factors like moisture, heat, and UV radiation, understanding the performance of materials used to protect these devices is critical. The degradation of these devices due to moisture ingress can be mitigated by developing methods to evaluate the moisture barrier properties of flexible encapsulant and edge seal materials, and using these methods to select materials appropriate for flexible packaging. Additionally, the mechanical adhesion performance of these materials is a critical property that must be understood in order to maximize the reliability of flexible devices. As a research contribution, this thesis evaluated a variety of encapsulant materials as well as an edge seal material for use in flexible PV packaging. By doing so, this work made original contributions by addressing the following questions:

- Which commercially available encapsulant and edge seal materials are capable of provide moisture ingress protection to PV modules, particularly through the sides of the module? What methods are available to accurately evaluate a variety of classes of materials?
- Of the high performing materials from moisture permeation studies, which can provide sufficient mechanical support to a device constructed using flexible materials, and how does this performance degrade as a result of environmental exposure?

To answer these questions, the properties of encapsulants and edge seals were investigated throughout this work, and the contributions achieved are:

- Chapter 2 investigated the moisture permeation properties of the materials in question using optical calcium degradation experiments. Specifically, samples were constructed that isolated the side permeation behavior of these materials. These experiments required high accuracy measurements during experiments that could last hundreds of hours, which necessitated the development of an automatic measurement system. Using MATLAB, accurate measurements of moisture permeation could be made rapidly without the need for hand measurements as had been standard in prior work. This method also provides an improvement in measurement resolution from ±0.5mm to ±0.01mm, which allows for measurement of increasingly high performance materials. The results of the moisture permeation study showed that desiccant-filled PIB based edge seal materials provide the best moisture protection by far, while the encapsulant materials do little to prevent moisture ingress. Of the encapsulant materials investigated, PDMS based formulations showed the highest rates of moisture ingress, while EVA and ionomer formulations performed modestly better. Since encapsulants do not provide meaningful moisture protection, the mechanical integrity of the edge seal material is critically important.
- Chapter 3 investigated the mechanical adhesion performance of encapsulants and edge seals in flexible architectures. Based on the results of the moisture permeation study, Qsil, EVA, PV5400, and ADCO were selected for evaluation. However, the initial adhesion strength to PET substrates was very poor for Qsil

and PV5400, so these materials were eliminated from further study at this time. The remaining materials, EVA and ADCO, were subjected to UV, thermal, and damp heat exposure. Using peel tests, it was found that some UV exposure can provide useful strengthening to the EVA/PET interface, while extended exposure weakens the bond; this was attributed to a polymerization followed by oxidation reaction, but it was found that the weakening can be mitigated by using a UV-blocking material. The ADCO/PET interface was initially weakened by UV radiation, but extended exposure strengthened the interface enough to cause cohesive failure. Thermal aging of the EVA/PET interface did not have dramatic effects on the strength, but chemical analysis showed evidence of oxidation. The ADCO/PET interface was dramatically weakened, but more work is needed to identify the underlying mechanism. Damp heat aging of the EVA/PET interface strengthened the bond due to a hydrolysis/condensation reaction, though this is not expected to be sustained in longer experiments. Damp heat aging of the ADCO/PET produced results similar to the thermal study.

Overall, it was found that several commercially available materials can be used in flexible PV packaging to provide good moisture protection as well as robust mechanical support. While flexible PV remain the minority in the industry, the technology continues to show strong potential for the future development of lightweight, low-cost, flexible devices. This work contributes to this goal by addressing several of the top reliability concerns, but continued efforts are needed to realize the potential of this technology. To this end, recommendations for future work are presented.

4.1 Future Work

4.1.1 Additional Moisture Permeation Studies

While Chapter 2 provided insight to the moisture barrier performance of a variety of materials, this work focused on a single aging condition. To fully understand the performance of these materials, multiple temperature and humidity conditions must be used. By doing so, the activation energy as well as an Arrhenius relationship can be determined, both of which are useful for further investigation and modelling of each material. This level of analysis would complement some of the recent work by Kempe *et al.* [25, 32]. Furthermore, other aging conditions such as thermal and UV exposure can be used to investigate the effects on moisture permeation.

Additionally, the optical calcium measurement technique can be extended to investigate architectures using barrier films. Materials like the 3M Ultra Barrier Film, and films like those developed by Hyung Chul Kim described previously, could be studied in tandem with the encapsulant and edge seal materials. This would provide a more comprehensive look at the entire device package. To this end, the materials identified in this work could be further investigated by integrating them into flexible devices. This would lead to more complex studies involving device/packaging interactions.

4.1.2 Additional Adhesion Studies

Chapter 3 investigated the mechanical performance of EVA and ADCO, as well as the degradation due to aging conditions. However, the results described in this work reflect relatively short experiments and isolated aging conditions. Therefore, it would be valuable

to extend and accelerate adhesion studies performed here to reflect the intended device lifetime.

In addition to degradation studies, work should be conducted to investigate how adhesion can be improved. For example, to improve encapsulant/PET adhesion, an inorganic adhesion layer could provide a more suitable surface. Some preliminary work has been performed in this area, and the results are reported in Table 12 below.

Table 12: Peel strength using an inorganic adhesion layer.

Adhesive	Substrate	Peel Strength (N/mm)
PV5400 Ionomer	PET	0.021 ± 0.002
Qsil (PDMS)	PET	0.022 ± 0.003
PV5400 Ionomer	ITO/PET	0.054 ± 0.007
Qsil (PDMS)	ITO/PET	0.046 ± 0.002

Using the low adhesion encapsulants from Chapter 3, peel samples were constructed using indium tin oxide (ITO) coated PET. It was found that peel strength increased by over 100%, but was still far too low to be of use in a device package. Other inorganic layers such as silicon nitride or silicon dioxide are more glass-like, and may provide better performance.

REFERENCES

[1] Feldman, D.J., Margolis, Robert M, and Hoskins, Jack, *Q4 2017/Q1 2018 Solar Industry Update*. 2018, National Renewable Energy Lab. (NREL), Golden, CO (United States).

[2] Lacal Arantegui, R. and A. Jäger-Waldau, *Photovoltaics and wind status in the European Union after the Paris Agreement.* Renewable and Sustainable Energy Reviews, 2018. **81**: p. 2460-2471.

[3] Sharma, V. and S.S. Chandel, *Performance and degradation analysis for long term reliability of solar photovoltaic systems: A review.* Renewable and Sustainable Energy Reviews, 2013. **27**: p. 753-767.

[4] Li, Y., et al., *Flexible and Semitransparent Organic Solar Cells.* Advanced Energy Materials, 2018. **8**(7): p. 1701791.

[5] Krebs, F.C., et al., *A round robin study of flexible large-area roll-to-roll processed polymer solar cell modules.* Solar Energy Materials and Solar Cells, 2009. **93**(11): p. 1968-1977.

[6] Li, G., et al., *High-efficiency solution processable polymer photovoltaic cells by self-organization of polymer blends.* Nature Materials, 2005. **4**(11): p. 864-868.

[7] Li, G., R. Zhu, and Y. Yang, *Polymer solar cells.* Nature Photonics, 2012. **6**(3): p. 153-161.

[8] Huang, Y.-C., et al., *Morphological control and performance improvement of organic photovoltaic layer of roll-to-roll coated polymer solar cells.* Solar Energy Materials and Solar Cells, 2016. **150**: p. 10-18.

[9] Peters, C.H., et al., *High Efficiency Polymer Solar Cells with Long Operating Lifetimes.* Advanced Energy Materials, 2011. **1**(4): p. 491-494.

[10] Sánchez-Friera, P., et al., *Analysis of degradation mechanisms of crystalline silicon PV modules after 12 years of operation in Southern Europe.* Progress in Photovoltaics: Research and Applications, 2011. **19**(6): p. 658-666.

[11] M.A. Quintana, D.L.K., T.J. McMahon, C.R. Osterwald, *Commonly Observed Degradation in Field-aged Photovoltaic Modules*, in *Twenty-Ninth IEEE Photovoltaic Specialists Conference*. 2002, IEEE: New Orleans, LA, USA.

[12] Kempe, M., *Modeling of rates of moisture ingress into photovoltaic modules.* Solar Energy Materials and Solar Cells, 2006. **90**(16): p. 2720-2738.

[13] Oliveira, M.C.C.d., et al., *The causes and effects of degradation of encapsulant ethylene vinyl acetate copolymer (EVA) in crystalline silicon photovoltaic modules: A review.* Renewable and Sustainable Energy Reviews, 2018. **81**: p. 2299-2317.

[14] Pern, J. *Module Encapsulant Materials, Processing and Testing*. in *APP International PV Reliability Workshop*. 2008. SJTU, Shanghai, China.

[15] M.D. Kempe, A.A.D., T.J. Moricone, and M.O. Reese. *Evaluation and Modeling of Edge-Seal Materials for Photovoltaic Applications*. in *IEEE Photovoltaic Specialists Conference (PVSC '10)*. 2010. Honolulu, Hawaii.

[16] Rance, W.L., et al., *The use of Corning® Willow™ glass for flexible CdTe solar cells*, in *IEEE 39th Photovoltaic Specialists Conference*. 2013, IEEE: Tampa, FL, USA.

[17] Peng, C.Y., et al., *Flexible CZTS Solar Cells on Flexible Corning® Willow® Glass Substrates*, in *IEEE 40th Photovoltaic Specialists Conference*. 2014, IEEE: Denver, CO, USA.

[18] Assche, F.v., et al. *Thin-film Barrer on Foil for Organic LED Lamps*. in *AIMCAL Fall Conference*. 2008.

[19] Galagan, Y., et al., *Roll-to-Roll Slot-Die Coated Organic Photovoltaic (OPV) Modules with High Geometrical Fill Factors.* Energy Technology, 2015. **3**(8): p. 834-842.

[20] Galagan, Y., et al., *Toward fully printed Organic Photovoltaics: Processing and Stability*, in *Lope-C*. 2010: Messe Frankfurt, Germany.

[21] Galagan, Y., et al., *ITO-free flexible organic solar cells with printed current collecting grids.* Solar Energy Materials and Solar Cells, 2011. **95**(5): p. 1339-1343.

[22] Jordan, D.C., et al., *Compendium of photovoltaic degradation rates.* Progress in Photovoltaics: Research and Applications, 2016. **24**(7): p. 978-989.

[23] Coyle, D.J., *Life prediction for CIGS solar modules part 1: modeling moisture ingress and degradation.* Progress in Photovoltaics: Research and Applications, 2013. **21**(2): p. 156-172.

[24] Coyle, D.J., et al., *Life prediction for CIGS solar modules part 2: degradation kinetics, accelerated testing, and encapsulant effects.* Progress in Photovoltaics: Research and Applications, 2013. **21**(2): p. 173-186.

[25] Kempe, M.D., et al., *Moisture ingress prediction in polyisobutylene-based edge seal with molecular sieve desiccant.* Progress in Photovoltaics: Research and Applications, 2018. **26**(2): p. 93-101.

[26] Jordan, D.C., et al., *Photovoltaic failure and degradation modes.* Progress in Photovoltaics: Research and Applications, 2017. **25**(4): p. 318-326.

[27] John H. Wohlgemuth, P.H., Nick Bosco, David C. Miller, Michael D. Kempe, Sarah R. Kurtz, *Assessing the Causes of Encapsulant Delamination in PV Modules*, in *IEEE 43rd Photovoltaic Specialists Conference (PVSC)*. 2016, IEEE: Portland, OR, USA.

[28] Jorgensen, G., et al., *Materials Testing for PV Module Encapsulation*, in *National Center for Photovolatics and Solar Program Review Meeting*. 2003: Denver, Co, USA.

[29] Munoz, M.A., et al., *Early degradation of silicon PV modules and guaranty conditions.* Solar Energy, 2011. **85**(9): p. 2264-2274.

[30] Kim, Y., et al., *Durable polyisobutylene edge sealants for organic electronics and electrochemical devices.* Solar Energy Materials and Solar Cells, 2012. **100**: p. 120-125.

[31] Kempe, M.D., A.A. Dameron, and M.O. Reese, *Evaluation of moisture ingress from the perimeter of photovoltaic modules.* Progress in Photovoltaics: Research and Applications, 2014. **22**(11): p. 1159-1171.

[32] Kempe, M.D., et al., *Modeling moisture ingress through polyisobutylene-based edge-seals.* Progress in Photovoltaics: Research and Applications, 2015. **23**(5): p. 570-581.

[33] Kim, H., *Investigation of ALD Thin Films to Improve the Reliability of Organic Electronic Devices* 2015, Georgia Institute of Technology. p. 223.

[34] Bosco, N., et al., *Defining Threshold Values of Encapsulant and Backsheet Adhesion for PV Module Reliability.* IEEE Journal of Photovoltaics, 2017. **7**(6): p. 1536-1540.

[35] Tracy, J., et al., *Encapsulation and backsheet adhesion metrology for photovoltaic modules.* Progress in Photovoltaics: Research and Applications, 2017. **25**(1): p. 87-96.

[36] Nick Bosco, J.T., Reinhold Dauskardt, Sarah Kurtz, *Development and First Results of the Width-Tapered Beam Method for Adhesion Testing of Photovoltaic Material Systems*, in *IEEE 43rd Photovoltaic Specialists Conference (PVSC)*. 2016, IEEE: Portland, OR, USA.

[37] Cai, C., et al., *Degradation of thermally-cured silicone encapsulant under terrestrial UV.* Solar Energy Materials and Solar Cells, 2016. **157**: p. 346-353.

[38] Novoa, F.D., D.C. Miller, and R.H. Dauskardt, *Adhesion and debonding kinetics of photovoltaic encapsulation in moist environments.* Progress in Photovoltaics: Research and Applications, 2016. **24**(2): p. 183-194.

[39] Kempe, M., et al., *Investigation of a wedge adhesion test for edge seals*, in *SPIE Optics + Photonics for Sustainable Energy*. 2016: San Diego, CA, USA.

[40] Kempe, M., et al., *Using a butt joint test to evaluate photovoltaic edge seal adhesion.* Energy Science & Engineering, 2019. **7**(2): p. 354-360.

[41] D3762-03, A., *Standard Test Method for Adhesive-Bonded Surface Durability of Aluminum (Wedge Test)*. 2010.

[42] Dupont, S.R., et al., *Adhesion properties of inverted polymer solarcells: Processing and film structure parameters.* Organic Electronics, 2013. **14**(5): p. 1262-1270.

[43] Dupont, S.R., et al., *Interlayer adhesion in roll-to-roll processed flexible inverted polymer solar cells.* Solar Energy Materials and Solar Cells, 2012. **97**: p. 171-175.

[44] Rolston, N., et al., *Mechanical integrity of solution-processed perovskite solar cells.* Extreme Mechanics Letters, 2016. **9**: p. 353-358.

[45] Cheacharoen, R., et al., *Design and understanding of encapsulated perovskite solar cells to withstand temperature cycling.* Energy & Environmental Science, 2018. **11**(1): p. 144-150.

[46] *Qsil 216 Technical Data Sheet*. 2017, Quantum Silicones.

[47] *2538 Silicone Encapsulant for PV Cells*. 2017, H.B. Fuller.

[48] *Dow Corning PV-6212 Cell Encapsulant*. 2014, Dow Corning.

[49] *PHOTOCAP 15580P*. 2015, STR Solar.

[50] *DuPont PV5400 Series*. 2013, DuPont.

[51] *HelioSeal PVS101*. 2011, H.B. Fuller.

[52] Nisato, G., Bouten, P.C.P., Slikkerveer, P.J., Bennett W.D., Graff, G.L., Rutherford, N., Wiese, L. *Evaluating High Performance Diffusion Barriers: The Calcium Test*. in *Asia Display/IDW*. 2001.

[53] Nisato, G., et al., *Experimental comparison of high-performance water vapor permeation measurement methods.* Organic Electronics, 2014. **15**(12): p. 3746-3755.

[54] Nissen, D.A., *The Low-Temperature Oxidation of Calcium by Water Vapor.* Oxidation of Metals, 1977. **11**.

[55] Otsu, N., *A Threshold Selection Method from Gray-Level Histograms.* IEEE Transactions on Systems, Man, and Cybernetics, 1979: p. 62-66.

[56] Paul, D.R., *Effect of Immobilizing Adsorption on the Diffusion Time Lag.* Journal of Polymer Science, 1969. **7**: p. 1811-1818.

[57] D. R. Paul, D.R.K., *The Diffusion Time Lag in Polymer Membranes Containing Adsroptive Fillers.* Journal of Polymer Science, 1973: p. 79-93.

[58] Cording, C.R., *Optimizing photovoltaic module glass reliability.* 2008. **7048**: p. 70480J.

[59] Films, D.T., *Melinex ST505*, in *Datasheet*. 2005.

[60] Kempe, M.D., *Ultraviolet light test and evaluation methods for encapsulants of photovoltaic modules.* Solar Energy Materials and Solar Cells, 2010. **94**(2): p. 246-253.

[61] Jorgensen, T.J.M.a.G.J., *Adhesion and Thin-Film Module Reliability*, in *IEEE 4th World Conference on Photovoltaic energy Conference*. 2006, IEEE: Waikoloa, HI, USA.

[62] Hah, J., *Encapsulation and Design of Scalable Packaging Materials for thin Film Perovskite Solar Cell Materials*, in *Materials Science and Engineering*. 2019, Georgia Institute of Technology.

[63] Uchida, E., Y. Uyama, and Y. Ikada, *Surface Graft Polymerization of Acrylamide onto Poly(ethylene Terephthalate) Film by UV Irradiation.* Journal of Polymer Science Part A: Polymer Chemistry, 1989. **2**p. 527-537.

[64] Decker, C. and A.D. Jenkins, *Kinetic Approach of 02 Inhibition in Ultraviolet- and Laser-Induced Polymerizations.* Macromolecules, 1985. **18**(6).

[65] Jin, J., S. Chen, and J. Zhang, *UV aging behaviour of ethylene-vinyl acetate copolymers (EVA) with different vinyl acetate contents.* Polymer Degradation and Stability, 2010. **95**(5): p. 725-732.

[66] Dubey, V. and S.K.P.N.B.S.N. Rao, *Research Trends in the Degradation of Butyl Rubber.* Journal of Analytical and Applied Pyrolysis, 1995: p. 111-125.

[67] Walzak, M.J., et al., *UV and ozone treatment of polypropylene and poly(ethylene terephthalate).* Journal of Adhesion Science and Technology, 1995. **9**(9): p. 1229-1248.

[68] Rubino, M., et al., *Effect of chlorine dioxide gas on physical, thermal, mechanical, and barrier properties of polymeric packaging materials.* Journal of Applied Polymer Science, 2010. **115**(3): p. 1742-1750.

[69] Gotoh, K., A. Yasukawa, and Y. Kobayashi, *Wettability characteristics of PET films treated by atmospheric pressure plasma and ultraviolet excimer light*. Vol. 43. 2011.

[70] Pazur, R.J., *Activation energy of poly(isobutylene) under thermo-oxidative conditions from 40 to 100 °C.* Polymer Degradation and Stability, 2014. **104**: p. 57-61.

[71] Hawkins, W.L., et al., *The Effect of Carbon Black on Thermal Antioxidants for Polyethylene.* Journal of Applied Polymer Science, 1959. **1**(1): p. 37-42.